atmosphere

MDPI

Article

Evaluation of Global Climate and Storm-Resolving Model Representations of Mixed-Phase Clouds and Their Hemispheric Contrasts

Olimpia Bruno [1,2,3,*], Jonah K. Shaw [4,5,6], Trude Storelvmo [4,7] and Corinna Hoose [1]

[1] Institute of Meteorology and Climate Research Troposphere Research, Karlsruhe Institute of Technology, 78131 Karlsruhe, Germany
[2] Institute of Photogrammetry and Remote Sensing, Karlsruhe Institute of Technology, 78131 Karlsruhe, Germany
[3] Institute of Meteorology and Climate Research Atmospheric Trace Gases and Remote Sensing, Karlsruhe Institute of Technology, 76344 Eggenstein-Leopoldshafen, Germany
[4] Department of Geosciences, University of Oslo, 0371 Oslo, Norway
[5] Department of Atmospheric and Oceanic Sciences, University of Colorado Boulder, Boulder, CO 80309, USA
[6] Cooperative Institute for Research in Environmental Sciences, University of Colorado Boulder, Boulder, CO 80309, USA
[7] School of Business, Nord University, 8049 Bodø, Norway
* Correspondence: olimpia.bruno@kit.edu

Abstract

Mixed-phase clouds, in which liquid droplets and ice crystals coexist at temperatures between −38 °C and 0 °C, play a critical role in Earth's radiation budget. Here, we assess the ability of climate and storm-resolving models to represent mixed-phase cloud properties and their hemispheric contrasts as inferred from satellite observations. We compare observations from the Advanced Very High Resolution Radiometer (AVHRR) and the Moderate Resolution Imaging Spectroradiometer (MODIS) with one global climate model, the Community Atmosphere Model version 6, Oslo configuration (CAM6-Oslo), and three storm-resolving models: the ICOsahedral Non-hydrostatic model (ICON), the Simple Cloud-Resolving E3SM Atmosphere Model (SCREAM), and the Goddard Earth Observing System model (GEOS). Our results show that all models reproduce the geographic distribution of mixed-phase clouds but differ significantly in detail. CAM6-Oslo yields the closest agreement in hemispheric contrasts of supercooled liquid fraction and its relationship with the liquid effective radius. Our results highlight the role of aerosol–cloud interactions and microphysics schemes in determining model performance and demonstrate that storm-resolving models still do not overcome the challenge of representing mixed-phase clouds at global scales.

Keywords: mixed-phase clouds; aerosol–cloud interactions; climate and storm-resolving model evaluation

Academic Editor: Kostas Eleftheratos

Received: 17 December 2025
Revised: 23 January 2026
Accepted: 28 January 2026
Published: 31 January 2026

1. Introduction

Mixed-phase clouds, which contain both liquid droplets and ice crystals, exert a strong influence on Earth's radiation budget. Their radiative effect depends critically on the partitioning between liquid and ice: for the same water content, liquid clouds are optically thicker and reflect more solar radiation than ice clouds. However, the physical processes governing liquid–ice partitioning remain incompletely understood, and their representation in weather and climate models is still highly uncertain [1].

Uncertainty arises from the interplay of several factors, including temperature, vertical motion, the availability of aerosols acting as cloud condensation nuclei or ice-nucleating particles, and microphysical processes such as nucleation, riming, and secondary ice production [2,3]. These processes determine the supercooled liquid fraction (SLF), representing the amount of supercooled liquid water normalized by the total condensate. Because the SLF strongly affects cloud radiative forcing, evaluating how well models reproduce the SLF is essential for reducing uncertainties in climate projections.

Satellite observations have provided valuable insights into mixed-phase clouds. Active sensors such as CALIPSO (Cloud-Aerosol Lidar and Infrared Pathfinder Satellite Observation) have been widely used to assess cloud phase occurrence and phase partitioning [4,5]. Passive sensors, despite their limitations, offer broader spatial and temporal coverage. The synergistic use of active and passive satellite sensors has been widely employed to characterize phase partitioning in mixed-phase clouds as a function of temperature, cloud type, and geographical location [6–8]. Such approaches have also highlighted systematic differences between retrievals from the two sensor types, thereby improving the interpretation of observational results. Using observations from both active and passive satellite sensors, Bruno et al. (2021) [6] reported systematic hemispheric contrasts in the SLF: values were generally larger in the Southern than in the Northern Hemisphere, except for continental low-level clouds where the opposite pattern was found. Hemispheric differences in mixed-phase cloud phase partitioning have also been suggested by active-sensor satellite products and ground-based observations, which generally indicate a higher persistence of the liquid phase in the Southern Hemisphere (e.g., [9–12]). More recently, in situ observations have also indicated the presence of hemispheric asymmetries in mixed-phase cloud properties, with higher supercooled liquid fractions reported in the Southern Hemisphere compared to the Northern Hemisphere [13]. Such contrasts may reflect large-scale differences in aerosol environments [14–16] and cloud microphysical processes but remain poorly constrained at the global scale, particularly from passive satellite observations. Given the evidence of hemispheric contrasts in observations, an open question is whether current climate and storm-resolving models are able to reproduce these differences and which aspects of model formulation control their representation.

In global climate models, large-scale atmospheric circulation is explicitly simulated, while convection and cloud microphysical processes are parameterized. Storm-resolving models explicitly represent convection and mesoscale dynamics, offering a complementary perspective on cloud processes, although they remain limited by short simulation periods and simplified microphysics. Whether storm-resolving models can reproduce the hemispheric SLF contrasts observed in mixed-phase clouds has not yet been assessed. Comparing global climate and storm-resolving models against the same observational benchmarks allows us to evaluate whether increased dynamical resolution alone is sufficient to improve the representation of mixed-phase clouds.

To evaluate model performance against observations, we adopt the framework introduced by Cesana et al. (2015) [17], who used joint histograms of the SLF as a function of cloud-top temperature (CTT). This approach provides a consistent way to compare satellite retrievals and model outputs despite differences in native variables and resolution. In this work, we extend this method by introducing joint histograms of the SLF and averaged liquid effective radius ($\overline{r_{liq}}$). By explicitly linking phase partitioning to droplet size, these histograms provide information on cloud microphysical processes that is not captured by temperature-based diagnostics alone.

Building on Bruno et al. (2021) [6], the present study expands the analysis in two ways. First, we evaluate not only a global climate model—the Community Atmosphere Model version 6, Oslo configuration (CAM6-Oslo)—but also three storm-resolving models: the

ICOsahedral Non-hydrostatic model (ICON), the Simple Cloud-Resolving Energy Exascale Earth System Model Atmosphere Model (SCREAM), and the Goddard Earth Observing System model (GEOS). Second, we propose the SLF–$\overline{r_{liq}}$ diagnostic as a new benchmark for assessing cloud microphysics.

The objectives of this study are therefore:

- To provide updated reference values for mixed-phase cloud occurrence based on satellite observations and models;
- To assess the ability of global and storm-resolving models to reproduce hemispheric contrasts of mixed-phase clouds;
- To explore the potential of SLF–$\overline{r_{liq}}$ relationships as a benchmark for evaluating model microphysics schemes.

2. Datasets

In this paper, datasets derived from observations, a global climate model, and three global storm-resolving models were analyzed.

The observations included two passive satellite sensor-based datasets: Cloud_cci AVHRR-PMv3 (Cloud Climate Change Initiative Advanced Very High Resolution Radiometer; ref. [18,19]), with "PM" indicating the equatorial crossing time in the afternoon, and MCD06COSP_D3_MODIS (Moderate Resolution Imaging Spectroradiometer (Aqua/Terra) Cloud Properties Level 3 daily [20,21]).

Bruno et al. (2021) [6] compared cloud property datasets derived from observations acquired by the passive AVHRR sensor onboard NOAA polar-orbiting satellites with those obtained from the active CALIOP (Cloud-Aerosol Lidar with Orthogonal Polarization) instrument onboard the polar-orbiting CALIPSO (Cloud-Aerosol Lidar and Infrared Pathfinder Satellite Observation) satellite. The AVHRR-based datasets showed a warm bias in cloud-top temperature compared to CALIOP; furthermore, a thermodynamic phase mismatch was found with ∼9% of cloud tops retrieved as liquid by CALIOP being identified as ice in AVHRR-based datasets. Nevertheless, AVHRR-based datasets were shown to be able to reproduce the hemispheric contrasts from the active satellite sensor CALIOP. Because of their agreement and the more limited spatial coverage of active sensors compared to passive ones over the same time frame, this study includes the Cloud_cci v3 dataset, which represents the latest AVHRR-based product examined by Bruno et al. (2021) [6] (hereafter **AVHRR**), whose cloud phase is generated by an artificial neural network trained on AVHRR measurements to reproduce CALIOP cloud phase, producing binary cloud phase information.

The MCD06COSP_D3_MODIS product [20,21] was specifically developed to enable comparisons between MODIS observations and climate model outputs using the Cloud Feedback Model Intercomparison Project (CFMIP) Observation Simulator Package 2 (COSP2) [22], which is included in the global climate model (GCM) dataset used in this study. The MCD06COSP_D3_MODIS dataset provides MODIS measurements from the polar-orbiting Aqua and Terra satellites, aggregated to a coarser spatial resolution ($1^\circ \times 1^\circ$) during dataset processing. The cloud optical properties are retrieved by using only one channel (3.7 µm) instead of six. For brevity and readability, we hereafter refer to this dataset as **MODIS**.

The GCM dataset we analyzed here is the atmospheric component of the Norwegian Earth System Model version 2 (NorESM2), which is based on the Community Atmosphere Model Version 6 (CAM6; ref. [23]) and is hereafter referred to as **CAM6-Oslo**. CAM6-Oslo uses the OsloAero5.3 [24] aerosol scheme and aerosol–radiation–cloud interactions from [25] and is the only model in this work to treat aerosols interactively as possible cloud condensation nuclei and ice nucleating particles. This model is therefore expected to be able to reproduce cloud features better than models not accounting for the aerosol–cloud

interaction. We specifically used MODIS-like cloud fields from CAM6-Oslo produced by the COSP2 satellite simulator to provide the best comparison with passive satellite retrievals. This output is still referred to as CAM6-Oslo in this paper.

The three global storm-resolving model datasets we analyzed are part of the DYnamics of the Atmospheric general circulation Modeled On Non-hydrostatic Domains (DYAMOND) Winter project [26]: **ICON** (ICOsahedral Nonhydrostatic Model; ref. [27,28]), **SCREAM** (Simple Cloud-Resolving E3SM (Energy Exascale Earth System Model) Atmosphere Model; ref. [29]), and **GEOS** (Goddard Earth Observing System; ref. [30]). For consistency, the atmosphere-only experiments of all models were used in this study. Because this study focuses on mixed-phase clouds and the passive satellite sensors provide only cloud-top information, only the cloud-top information of model outputs was used, therefore reproducing the satellite view of clouds. The following cloud parameters were considered in this study: cloud-top phase (CPH) as either liquid or ice pixel (for AVHRR), liquid (CLW) and ice (CLI) cloud fraction (for MODIS and CAM6-Oslo), or mass mixing ratio of ice (q_i) and liquid water (q_l, for the DYAMOND datasets); cloud-top pressure (CTP); cloud-top temperature (CTT); cloud optical thickness (COT); and liquid cloud effective radius (r_{liq}) at the cloud top. Not all datasets provide all variables. These are listed in Table 1 for each dataset together with the most relevant features for our study.

Table 1. Overview of the datasets analyzed in this study. The names shown in bold indicate how each dataset is referred to throughout the manuscript. ATBD denotes the Algorithm Theoretical Basis Document.

Dataset	Sensor/Scheme	Source	Spatial Resolution	2D/3D	Time Resolution	Analyzed Period
Cloud_cci v3	**AVHRR**	NOAA-19	0.05° × 0.05°	2D	daily	June 2009–May 2013
MCD06COSP	**MODIS**	Aqua/Terra	1° × 1°	2D	daily	June 2009–May 2013
CAM6-Oslo	two-moment	NorESM model + COSP simulator	1.875° × 2.5°	2D	daily	June 2009–May 2013
ICON	single-moment	(storm-resolving) DYAMOND model	5 km	3D	3 h	February 2020
SCREAM	two-moment	(storm-resolving) DYAMOND model	3.25 km	3D	3 h	February 2020
GEOS	single-moment	(storm-resolving) DYAMOND model	3 km	3D	3 h	February 2020

Dataset	Cloud parameters	Cloud phase	SLF Metric	Reference
AVHRR	CPH, CTT, CTP, COT, r_{liq}	liquid or ice	Equation (1)	Stengel et al. (2020) [18], ATBD [19]
MCD06COSP	CLW, CLI, CTP, COT, r_{liq}	liquid and ice cloud fraction	Equation (2)	Pincus et al. (2022) [20], NASA MCD06COSP_D3_MODIS [21]
CAM6-Oslo	CLW, CLI, CTT, CTP, COT, r_{liq}	liquid and ice cloud fraction	Equation (2)	Seland et al. (2020) [23]; COSP: Bodas-Salcedo et al. (2011) [22]
ICON	q_i, q_w, CTT, CTP	cloud mass fraction of ice and liquid water	Equation (3)	DWD ICON/ICON-EPS Database [27], Zängl et al. (2015) [28]
SCREAM	q_i, q_w, CTT, CTP, COT	cloud mass fraction of ice and liquid water	Equation (3)	Caldwell et al. (2021) [29]
GEOS	q_i, q_w, CTT, CTP, r_{liq}	cloud mass fraction of ice and liquid water	Equation (3)	Putman and Suarez (2011) [30]

3. Methods

All datasets provide global data with daily or higher time resolution, here analyzed near-globally (60° N to 60° S), excluding satellite observations with low confidence caused by sea ice coverage [31] and high solar zenith angle [32]. Alongside the near-global analysis, continental and marine regions were analyzed separately, together with different cloud types and latitudinal ranges: Northern Hemisphere (NH) mid-latitudes from 60° N to 30° N and Southern Hemisphere (SH) mid-latitudes from 30° S to 60° S. We analyzed 4 years (from 1 June 2009 to 31 May2013) of AVHRR, MODIS, and CAM6-Oslo; during this period, AVHRR has been validated in the mixed-phase temperature range on a near-global scale [6], supporting the reliability of these data for this study. The DYAMOND datasets, however, which are computationally very costly, are only available for a 30-day analysis period (30 January–28 February 2020) following a 10-day spin-up period. In this study, only the February portion is used. The temporal mismatch between the DYAMOND datasets and the other datasets represents a limitation of the present study and may introduce seasonal sampling effects that should be considered when interpreting the results.

3.1. Cloud Identification

AVHRR, MODIS, and the COSP outputs from CAM6-Oslo provided cloud-top data represented in two-dimensional latitude–longitude composites, while the DYAMOND datasets provided a three-dimensional atmospheric perspective. For this reason, a top-down approach was used to identify cloud tops in the DYAMOND models. For ICON and GEOS, the cloud top was determined as the uppermost layer where $q_w + q_i > 10^{-8}$ kg kg^{-1}, following [33]; to make SCREAM data consistent with ICON and GEOS, the cloud top was defined as the highest layer where COT > 0.

We also wish to account for the diurnal and COT-dependent sampling characteristics of AVHRR and MODIS when producing comparable model fields with CAM6-Oslo. Specifically, the analysis of AVHRR and MODIS was restricted to daytime observations since COT relevant for cloud-type classification can only be retrieved in the visible spectrum. To exclude very thin clouds with higher retrieval uncertainty, only satellite measurements with COT > 0.3 and effective radius > 4 µm were considered in this study [34]. For consistency, the same filters were applied to CAM6-Oslo, with the cloud top being defined as the highest cloud layer below an overlying COT of 0.3 for the COSP outputs.

3.2. SLF Derivation

The SLF was computed at the top of mixed-phase clouds. As in AVHRR the thermodynamic phase of each cloudy pixel is restricted to either liquid or ice, and it was necessary to reduce the spatial resolution in order to compute the SLF at the gridbox scale: The original latitude–longitude daily composites consisting of 3000 × 7200 pixels (0.05° spatial resolution) were reorganized into 500 × 1200 gridboxes of 6x6 pixels (0.3° spatial resolution), with each gridbox classified as cloudy only when at least two cloudy pixels were present (corresponding to more than ∼5.56% cloud coverage within the gridbox). Furthermore, the gridboxes were only included in the analysis if the largest difference between the coldest and the warmest cloud-top temperature of all valid pixels was less than 20 °C, filtering out gridboxes including clouds of very different heights (such as low- and high-level clouds; ref. [6]). Finally, gridboxes were identified as mixed-phase if they included coexisting liquid and ice pixels with a cloud-top temperature between −40 °C and 0 °C. For each gridbox, the SLF computation is based on the number of liquid and ice pixels in the gridbox, following Equation (1):

$$SLF_{n^\circ\ pixel} = \frac{\text{n}^\circ \text{ liquid pixels}}{\text{n}^\circ \text{ liquid pixels} + \text{n}^\circ \text{ ice pixels}} \quad (1)$$

Both MODIS and the model datasets provide information on both liquid and ice content or cloud fraction in each pixel. Consequently, no spatial aggregation into gridboxes was required for the computation of the SLF since mixed-phase conditions can already be represented at the individual pixel level. Hence, the SLF was computed as the ratio between the liquid cloud fraction and the total cloud fraction (liquid plus ice) for MODIS and CAM6-Oslo (Equation (2)) or as the ratio between the liquid water mass mixing ratio and the total mass mixing ratios of liquid and ice water for ICON, SCREAM, and GEOS (Equation (3)).

$$SLF_{cloud\ fraction} = \frac{\text{liquid cloud fraction}}{\text{liquid cloud fraction} + \text{ice cloud fraction}} \tag{2}$$

$$SLF_{mass\ fraction} = \frac{q_w}{q_w + q_i} \tag{3}$$

Hoose et al. (2018) [35] applied a comparable approach to derive the cloud top liquid fraction from models and found that $SLF_{n^\circ\ pixel}$ was 1 °C to 2 °C warmer than $SLF_{mass\ fraction}$ at SLF $\sim$ 0.5. This result suggests that these metrics are generally comparable, though $SLF_{mass\ fraction}$ may be slightly higher than $SLF_{n^\circ\ pixel}$.

ICON, SCREAM, and GEOS were analyzed after coarse graining to 0.5° × 0.5° by averaging for better comparison with AVHRR.

3.3. Classification of Cloud Regimes and k-Means Clustering

The clustering of clouds into groups called *regimes* is a widely used method over the last few decades. In some works the classification is based on vertical velocity [36,37], on sea level pressure [38], or on sea surface temperature and large-scale vertical motion [39–41], and in some others on CTP, COT, and total cloud cover [42–48]. Our cloud-type classification was based on standard ISCCP (International Satellite Cloud Climatology Project) cloud-top pressure (CTP = $[0, 440, 680, 1000]$ hPa) and cloud optical thickness (COT = $[0, 3.6, 23, 379]$) thresholds, as in Bruno et al. (2021) [6]. Each COT-CTP combination was associated with a corresponding cloud-type label (e.g., cumulus or altocumulus [49]). Since cloud-type classifications relying exclusively on COT and CTP are known to have limitations [50], the cloud names are mainly used as a reference to compare clouds within the same COT-CTP ranges. GEOS and ICON do not include COT information in the available datasets; therefore, their clouds were classified using CTP thresholds of $[0, 440, 680, 1000]$ hPa to classify them into high-, mid-, and low-level clouds. SCREAM provides COT values for each vertical level, but the column-integrated COT was used for each location.

As the spatial resolution of AVHRR and DYAMOND datasets has been coarsened (Section 3.2), pixel-based COT and CTP information in the original resolution has been collected in COT-CTP joint histograms. While the clouds from the MODIS and CAM6-Oslo could be directly classified at the pixel level using COT-CTP joint histograms, DYAMOND datasets and AVHRR required a different approach since COT and CTP information was already aggregated into joint histograms. Therefore, k-means clustering was applied to the joint histograms to classify cloud regimes in the AVHRR and DYAMOND datasets.

The k-means algorithm [51] partitions data points or vectors into clusters by minimizing the sum of squared Euclidean distances between each point and the corresponding cluster centroid. However, the method is subject to several limitations, for instance when clusters are widely separated and centroids are unable to transition between them or when stable, high-density clusters constrain centroid movement, potentially leading to an over-representation of dense regions at the expense of sparser clusters. An additional challenge in cluster analysis is the determination of an appropriate number of clusters that adequately

represents the data. These issues can be mitigated through improved centroid initialization and by repeating the k-means procedure using different initial configurations [52].

Initializing 42 centroids for AVHRR allowed all possible COT–CTP combinations to be represented, excluding cases with COT < 0.3 in accordance with the applied filtering for satellite observations and the simulator. Specifically, the COT–CTP space was discretized into 6×7 bins, defined by COT $= [0.3, 1.3, 3.6, 9.4, 23, 60, 379]$ and CTP $= [0, 180, 310, 440, 560, 680, 800, 1000]$ hPa, respectively. This choice rendered the k-means clustering deterministic. As a result, the likelihood of overlooking specific cloud types was minimized, low-density clusters were retained unless empty, and repeated k-means iterations were unnecessary since identical initial centroids lead to identical final clusters.

Following the same rationale, seven predefined initial centroids—corresponding to the number of CTP bins—were used to cluster the CTP histograms for ICON and GEOS. For SCREAM, 49 initial clusters (7 COT times 7 CTP combinations) were employed as no COT-based filtering was applied to this dataset (see Section 3.1).

The resulting clusters were subsequently merged to obtain the final nine cloud types [49] or, alternatively, to group them into three cloud-height categories. To this end, each cluster was assigned to a cloud type based on its most frequent COT–CTP combination. After this classification step, the nine final COT–CTP joint histograms and the three CTP histograms were individually normalized, each representing a distinct cloud type.

3.4. Geographical Distributions and Joint Histograms

After completing the cloud classification and computing the SLF, we derived the spatial distribution as well as the joint histograms of SLF–CTT and SLF–$\overline{r_{liq}}$ for each cloud type.

We defined the relative frequency of occurrence of all clouds (H_{all}, Equation (4)) and mixed-phase clouds (H_{MP}, Equation (5)) as a percentage:

$$H_{all} = \frac{\text{n°cloudy pixels}}{\text{n°[cloudy + failing quality-control filters + clear sky] pixels}} \times 100 \quad (4)$$

$$H_{MP} = \frac{\text{n°mixed-phase cloudy pixels}}{\text{n°[cloudy + failing quality-control filters + clear sky] pixels}} \times 100 \quad (5)$$

where the pixels are replaced by gridboxes in AVHRR.

We also defined the geographical relative frequency of occurrence of a cloud category $H_{geo_{i,j}}$, normalized by the number of total available observational or model output time steps (including cloud-free pixels) $N_{tot_{i,j}}$, for each latitude–longitude position and expressed it in percentage:

$$H_{geo_{i,j}} = \frac{N_{i,j}\ \text{(cloud category)}}{N_{tot_{i,j}}} \times 100, \quad (6)$$

where i and j represented the position in latitude and longitude of the geographical distribution, while the cloud category is the combination of height (high, middle, or low clouds) and thermodynamic phase (all or mixed-phase clouds).

The SLF-CTT joint histograms show for all cloud types the variation in the SLF with CTT, using a bin width of 0.05 for the SLF and 1 °C for CTT. For MODIS, CTT was replaced by CTP, spanning 0–1000 hPa with a bin width of 25 hPa. For each cloud type, we normalized the SLF-CTT histograms with their own total frequency of occurrence ($H_{k,l}$, Equation (7), where $N_{k,l}$ represents the absolute frequency of occurrence at bin combination (k,l), k denotes CTT or CTP, and l denotes the SLF). The SLF-$\overline{r_{liq}}$ joint histograms illustrate how $\overline{r_{liq}}$ changes with the SLF across all cloud types, providing insight into cloud dynamics and microphysical properties and complementing temperature-based diagnostics. These

histograms were normalized individually for each cloud type (Equation (7)), with k now referring to $\overline{r_{liq}}$.

$$H_{k,l} = \frac{N_{k,l}}{\sum_{k,l} N_{k,l}} \quad (7)$$

For consistency with Bruno et al. (2021) [6], we additionally normalized the histograms by applying a method analogous to CFAD (Contoured Frequency by Altitude Diagrams, $H_{CFADk,l}$, Equation (8)). CFAD histograms were originally proposed by Yuter and Houze (1995) [53] and have since been adapted for use in various subsequent studies (e.g., [54–57]). To highlight hemispheric contrasts in the SLF over land and ocean, we computed the difference of SLF-CTT histograms using the CFAD-like histograms.

$$H_{CFAD_{k,l}} = \frac{N_{k,l}}{\sum_{k} N_{k,l}} \quad (8)$$

A significance test based on the p-value had been applied to these histograms, showing dots where the bins showed a statistically significant difference between the NH and SH. The p-value had been calculated at the highest possible resolution, i.e., for each bin along with its eight neighboring bins. Consequently, bins located at the edges of the histograms could not undergo significance testing. The threshold for significance can be arbitrary; in this study, a value of 0.05 was adopted [58].

4. Results

4.1. Near-Global Cloud Cover and Mixed-Phase Occurrence

The relative frequencies of occurrence of all (H_{all}) and mixed-phase (H_{MP}) clouds retrieved from the datasets between 60° N and 60° S are presented in Table 2.

Table 2. Relative frequency of occurrence of all (H_{all}) and mixed-phase (H_{MP}) clouds and their ratios retrieved from all datasets included in this study between 60° N and 60° S for the period 1 June 2009 to 31 May 2013 for AVHRR, MODIS, and CAM6-Oslo and for February 2020 for ICON, SCREAM, and GEOS. In AVHRR, cloudy boxes and mixed-phase boxes were considered, and a pixel-wise amount of all clouds is also provided in parentheses.

Spatial Resolution	**AVHRR (0.05°) 0.3°**	**MODIS 1°**	**CAM6-Oslo 1.875° × 2.5°**	**SCREAM 0.5°**	**ICON 0.5°**	**GEOS 0.5°**
H_{all}	(59.2%) 52.9%	87.3%	71.7%	81.3%	65.5%	72.1%
H_{MP}	6.2%	55.0%	16.7%	3.1%	6.9%	14.7%
H_{MP}/H_{all}	11.7%	63.0%	23.3%	3.5%	10.5%	20.4%

The use of different sensors and models with individual characteristics; the application of different filters; the use of only daytime data (providing COT) in AVHRR, MODIS, and CAM6-Oslo; and the use of customized equations can lead to differences in the frequency of occurrence of clouds so that H_{all} is more consistent between the datasets than H_{MP}, partly due to resolution and the definition of "mixed-phase"; H_{all} of AVHRR decreases from 59.2% to 52.9% when the dataset is coarse-grained from 0.05° to 0.3° as a cloudy gridbox must contain at least two cloudy pixels; ICON shows the closest H_{all} (65.5%) and H_{MP} (6.9%) to the observations of AVHRR (52.9% and 6.2%, respectively). Figures 4–42 in the *Product Validation and Intercomparison Report—ESA Cloud_cci (2020)* [59] show the time series of the monthly cloud fraction (here H_{all}) for afternoon satellite retrievals, where it can be seen that the largest monthly differences within one year are mainly confined to a 5% range (and this is always the case considering, e.g., NOAA-19 only), so the large differences in H_{all} between the DYAMOND datasets (including only February) and the other datasets (including full years) are not expected to depend on the different time periods analyzed.

The observational datasets (AVHRR and MODIS) show large differences in both H_{all} and H_{MP}. This may be due to the use of only the 3.7 µm channel in MODIS to retrieve cloud optical properties, as well as the combination of daily time frames of Terra and Aqua observations to provide cloud-top-related parameters at the final $1^\circ \times 1^\circ$ spatial resolution. Previous validation studies including AVHRR (e.g., [6,18]) have shown the strong performance of this dataset compared to others derived from passive and active satellite sensors. In addition, H_{all} from AVHRR is closer to previous satellite studies (ranging from 61.9% to 67.2% for afternoon satellites; ref. [59]) than MODIS. For these reasons, we subsequently focus on the observational data from AVHRR and using the MODIS dataset for its intended comparisons with COSP outputs from CAM6-Oslo.

4.2. Geographical Distribution and Occurrence of Clouds

Figure 1 shows the relative frequency of occurrence of all clouds derived from AVHRR and MODIS, alongside four model datasets.

Cloud types at the same height are combined to obtain high-, mid-, and low-level clouds such that ICON and GEOS, which do not provide COT, can be included in the comparison. The relative frequency of occurrence H_{all} (calculated with Equation (4)) refers to CTP $>$ 680 hPa for low-level clouds, 440 hPa $<$ CTP $\leq$ 680 hPa for mid-level clouds, and CTP $<$ 440 hPa for high-level clouds, and it shows notable differences across datasets. AVHRR and MODIS retrieve a higher fraction of low-level clouds ($H_{all} = 37.83\%$ and 50.59%, respectively) compared to mid- ($H_{all} = 7.9\%$ and 19.3%) and high-level clouds ($H_{all} = 7.15\%$ and 17.41%). In contrast, most models exhibit a larger proportion of high-level clouds (H_{all} ranging from 27.17% to 52.06%) than low-level clouds (H_{all} ranging from 13.35% to 27.10%). Despite all these differences, which may also be related to the filter applied to COT for the cloud top definition used in AVHRR, MODIS, and CAM6-Oslo, the datasets analyzed indicate consistent spatial patterns in the vertical distribution of clouds. As shown in Figure 1, low-level clouds occur predominantly over oceanic regions, whereas clouds at medium and high altitudes are distributed over both land and sea, in agreement with previous findings [43,45,46,60]. More specifically, clouds at medium and high levels are most frequent in the extratropical regions and around the Intertropical Convergence Zone (ITCZ), which are areas often subject to synoptic- and mesoscale events. In contrast, low-level clouds are primarily observed over the oceans, particularly along their eastern boundaries, where they form below a capping inversion created by the atmospheric subsidence over low sea surface temperatures.

However, the geographical distributions also show differences between the datasets. For instance, AVHRR and MODIS show a more spatially extensive distribution of low-level clouds along the western margins of the ocean basins compared to the models, such as in the Pacific Ocean off the coast of South America. Conversely, SCREAM and GEOS simulate high-level clouds over the eastern Pacific near North America, where their occurrence is lower in AVHRR and MODIS and where such clouds are not detected in CAM6-Oslo and ICON. These discrepancies in the geographical distribution of clouds across datasets, combined with the differences observed in H_{all}, suggest that the vertical structure of clouds in the models may not be accurately represented. This interpretation is consistent with previous evaluations showing that global climate and weather models exhibit systematic biases in cloud vertical structure relative to satellite observations [61–63].

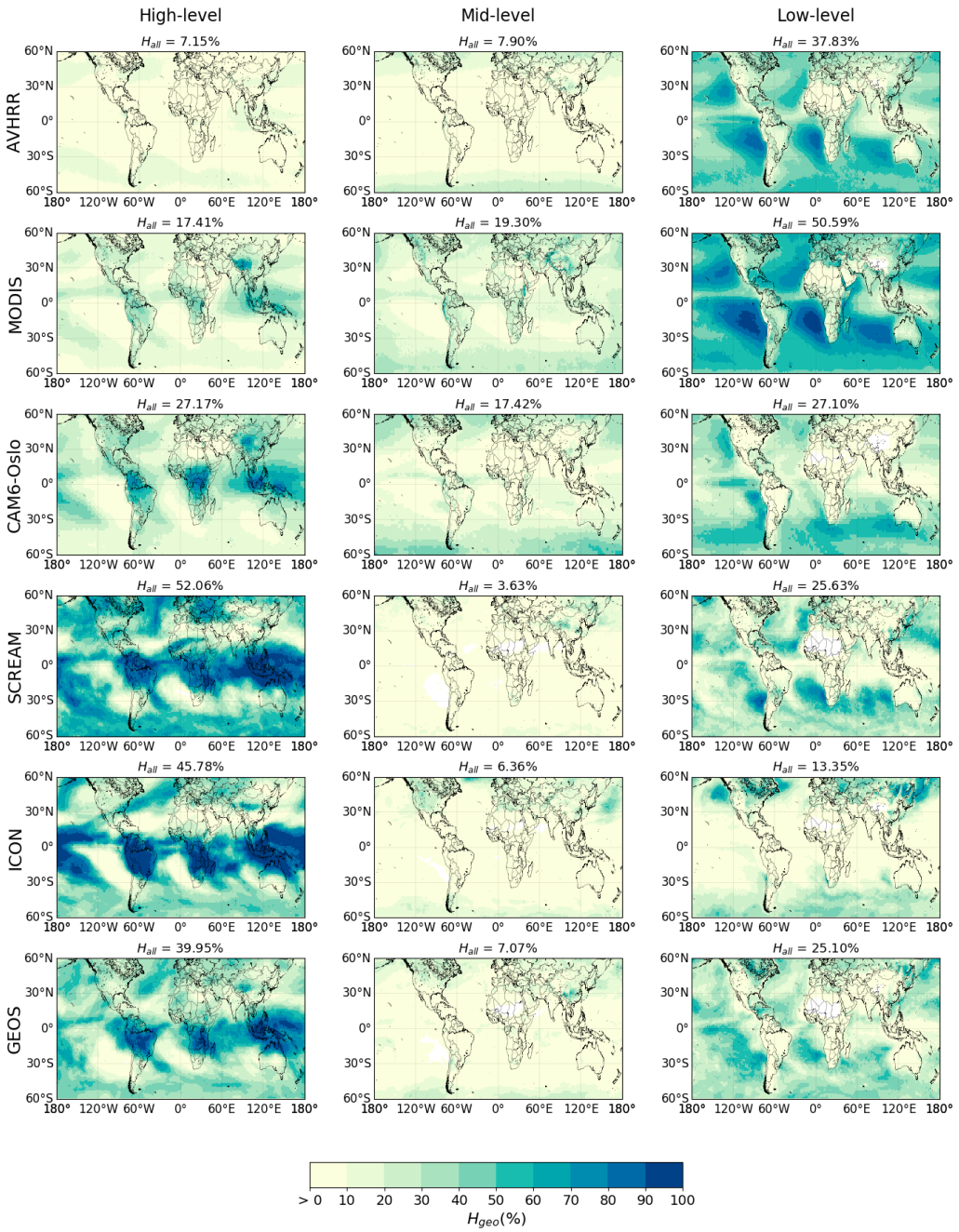

Figure 1. Geographical distribution of all cloud tops for the different datasets combined at three height levels: high- (left), mid-, and low-level (right). The relative frequency of occurrence (H_{all}, Equation (4)) is shown above each distribution. The color bar indicates the geographical frequency of occurrence H_{geo} (Equation (6)).

In Figure 2, the geographical distributions of mixed-phase clouds at the three cloud-height categories are illustrated for all datasets, analogously to Figure 1. Overall, the datasets exhibit similar large-scale spatial patterns, with mixed-phase clouds predominantly occurring in the mid-latitudes. Although mixed-phase clouds can be found at all latitudes [64], this behavior is consistent with the findings of Hu et al. (2010) [65], who reported the presence of supercooled liquid water in both convective and stratiform cloud systems in these regions.

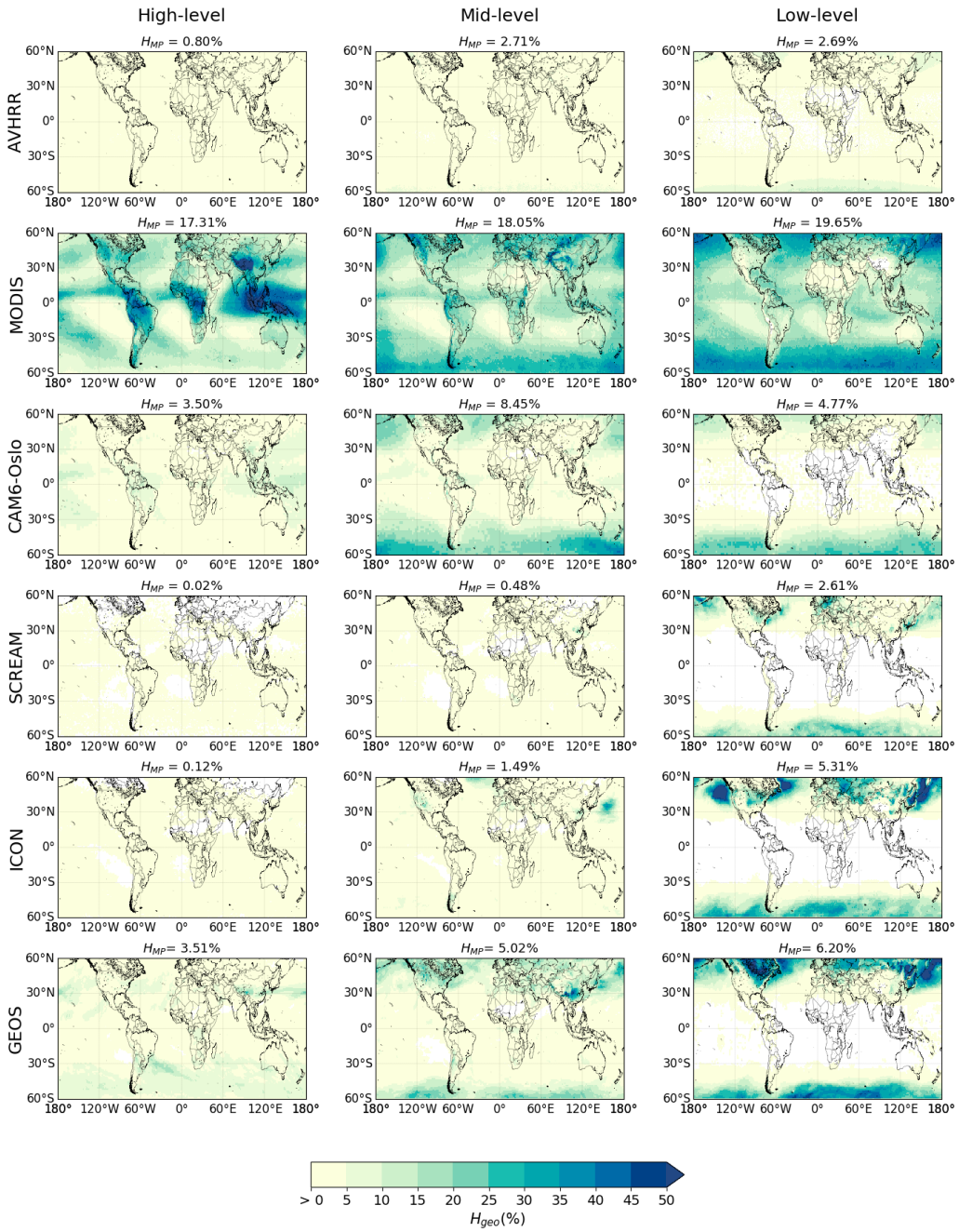

Figure 2. Geographical distribution of mixed-phase cloud tops for the different datasets combined at three height levels: high- (left), mid-, and low-level (right). The relative frequency of occurrence (H_{MP}, Equation (5)) is shown above each distribution. The color bar indicates the geographical frequency of occurrence H_{geo} (Equation (6)). Note that the color bar has a smaller range than in Figure 1.

Our results show that low-level clouds constitute the dominant contribution to the occurrence of mixed-phase clouds, except for AVHRR and CAM6-Oslo, for which mixed-phase clouds are mostly in the mid-level height, with H_{MP} of AVHRR in the mid-level being only 0.02% larger than in the low-level height. However, the MODIS product retrieves a higher frequency of mixed-phase clouds than the other datasets, with occurrences extending into the tropics in regions characterized by strong updrafts promoting the development of high-altitude clouds with ice cloud tops (e.g., the ITCZ). This behavior may partly reflect the MODIS retrieval strategy, which combines observations from Aqua and Terra to provide daily cloud properties at a spatial resolution of 1°. As a result, spatial averaging may

lead to the identification of mixed-phase conditions in grid boxes that include both liquid-topped and ice-topped clouds. This interpretation is consistent with in situ observations showing that mixed-phase clouds are highly heterogeneous at spatial scales smaller than typical satellite retrieval footprints, particularly in mid- and high-latitude clouds [66]. As a consequence, satellite products relying on spatial averaging may overestimate the occurrence of mixed-phase conditions within individual grid boxes—when separate cloud phases coexist—while also failing to capture part of the fine-scale mixed-phase structure. This limitation is particularly relevant when interpreting the geographical distribution of mixed-phase clouds, especially in regions dominated by deep convection, such as the tropics, where mixed-phase conditions may occur at scales smaller than the satellite pixel. The inter-model differences apparent in the geographical distributions in Figure 2 suggest variations in the simulated atmospheric dynamics, potentially resulting in regionally dependent cloud microphysical and macrophysical characteristics within the same cloud-height class. Figures 1 and 2 show different cloud locations depending on the datasets. Specific patterns in the DYAMOND models may be due to seasonal effects (e.g., boreal Winter storm track) or could suggest that the vertical structure of clouds in the models may not be accurately represented, as previously discussed for Figure 1.

4.3. Temperature Dependence of Mixed-Phase Cloud Types

Figure 3 illustrates the SLF-CTT joint histograms of the different cloud types for AVHRR normalized as in Equation (7).

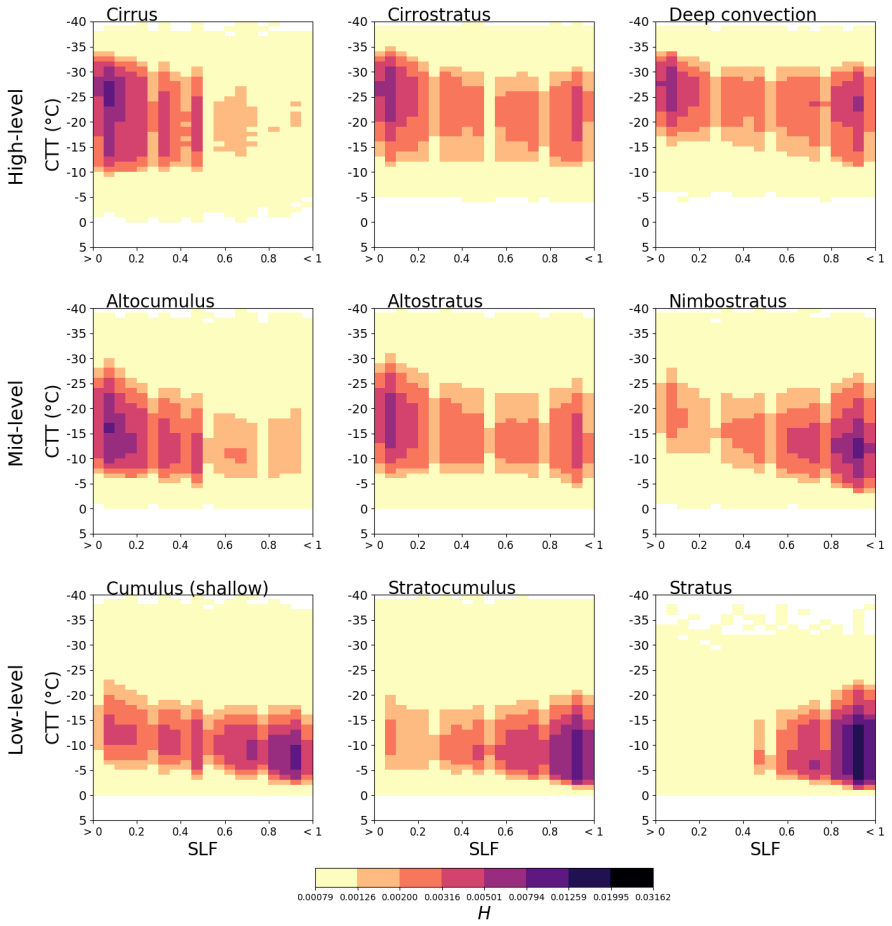

Figure 3. SLF−CTT joint histograms of mixed-phase clouds for AVHRR. The color bar indicates the frequency of occurrence H (Equation (7)) for a given SLF−CTT bin.

Each cloud type has a unique SLF-CTT joint histogram, reflecting cloud-specific processes that may be influenced by dynamical conditions or regional factors, such as variations in aerosol composition. As expected from the dependence of cloud-top temperature on cloud altitude, CTT decreases from low- to mid- and high-level clouds, and the SLF systematically declines with decreasing CTT. All datasets display these trends (Figures S1–S5) although the histograms appear very different at first sight. Within the temperature interval from -40 °C to 0 °C, the decrease in the SLF at lower temperatures may be associated with heterogeneous ice nucleation, secondary ice production, and the Wegener–Bergeron–Findeisen (WBF) process. For example, about 30% of all stratocumulus clouds have an SLF < 0.5, while only about 10% of stratus clouds have an SLF < 0.5, indicating very inefficient glaciation processes in stratus clouds compared to stratocumulus clouds or the possibility for stratus clouds to completely glaciate (very efficient glaciation processes) and quickly dissipate due to ice crystal sedimentation or snow. The occurrence of cirrus clouds within the mixed-phase cloud regime may arise from the cloud-type classification based on COT–CTP thresholds [50]. Previous studies (e.g., [67]) have shown the presence of supercooled liquid droplets in cirrus clouds. However, the presence of cirrus clouds at temperatures characteristic of heterogeneous glaciation processes, as in our results, suggests the presence of lower clouds in the cirrus regime and implies that this regime represents a mixture of clouds with CTP$<$ 440 hPa and COT < 3.6.

4.4. Hemispheric Differences of Continental and Maritime Mixed-Phase Clouds

Figure 4 shows, for all datasets, the hemispheric contrast for continental and maritime regions for only cirrostratus and stratocumulus clouds, which we found to generally be the most frequent cloud types in the mixed-phase for high- and low-level clouds, respectively (Table S1). An example of derivation of these difference plots between CFAD-like histograms is shown in Figure S6 for AVHRR.

For a given CTT < -15 °C in AVHRR (Figure 4, top row), cirrostratus clouds exhibit higher SLF values in the SH than in the NH over both land and oceanic regions, as indicated by the turquoise shading at a high SLF in the difference plot. A similar hemispheric contrast is found for stratocumulus clouds over oceanic regions. In contrast, stratocumulus clouds over land display the opposite behavior, with a higher SLF in the NH than in the SH for CTT warmer than approximately -20 °C, consistent with the findings of Bruno et al. (2021) [6].

Beyond Bruno et al. (2021), hemispheric asymmetries in mixed-phase phase partitioning have also been reported by other studies. In particular, analyses based on active satellite sensors cloud phase products indicate a higher persistence of the liquid phase in the SH compared to the NH at comparable temperatures [9,10], consistent with the contrasts identified here for cirrostratus and marine stratocumulus clouds (noting that these studies employ different phase metrics rather than the SLF). Recent in situ observations by Yang et al. (2025) [13] similarly report higher supercooled liquid fractions in the SH, providing independent qualitative support for the sign of the hemispheric contrast. However, the study of Yang et al. (2025) is based on localized aircraft observations and does not provide a near-global assessment stratified by cloud height and surface regime. As a result, the opposite hemispheric contrast identified here for continental stratocumulus clouds could not be directly evaluated in that study.

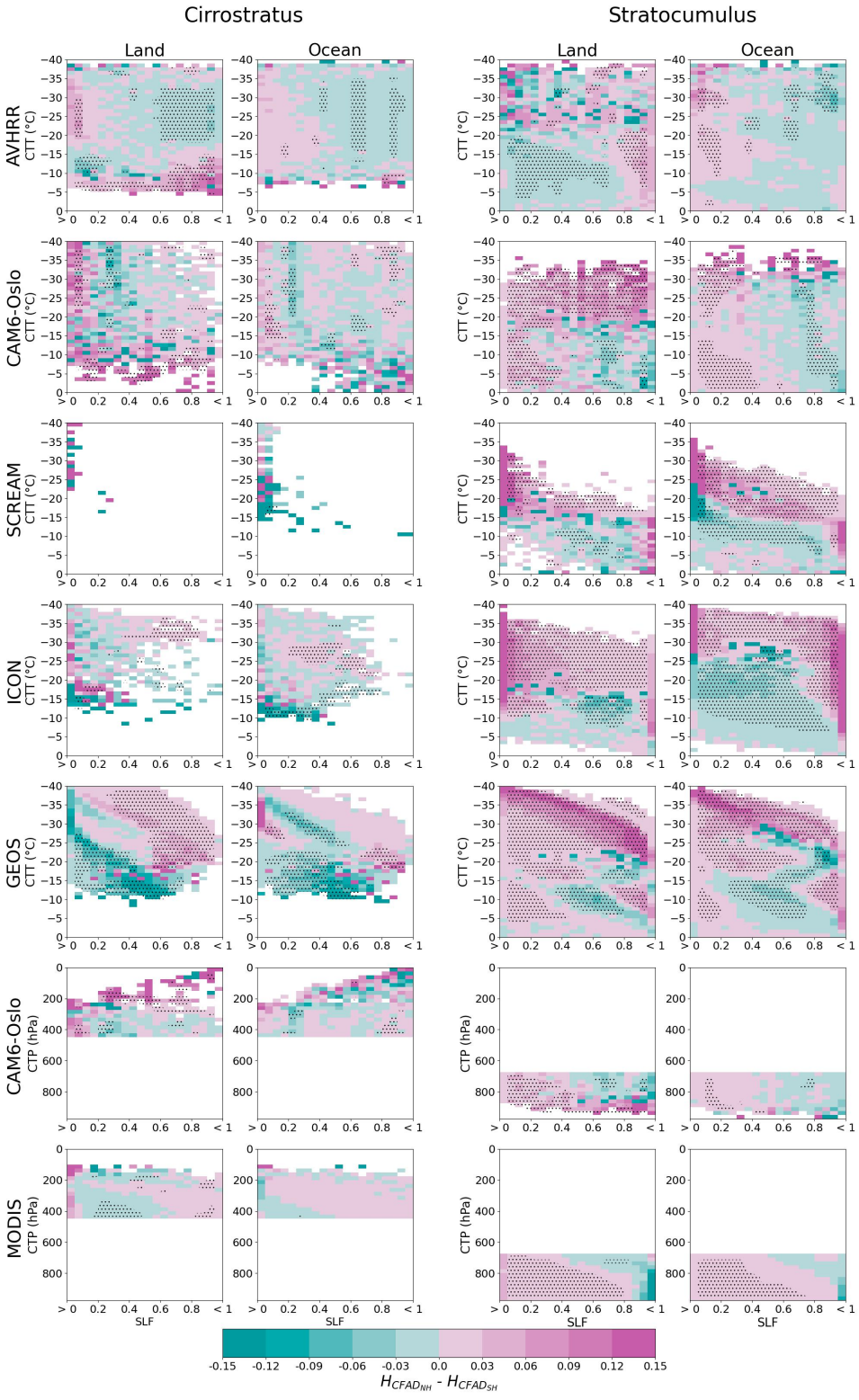

Figure 4. Hemispheric differences (NH minus SH) between CFAD−like histograms (Equation (8)) of cirrostratus or high-level clouds (left) and of stratocumulus or low-level clouds (right) over land and the ocean for all datasets. CFAD−like histograms of MODIS are derived from SLF−CTP histograms, while both SLF−CTP and SLF−CTT histograms are used to derive CFAD−like histograms of CAM6−Oslo. Cirrostratus clouds are replaced by high−level clouds for ICON and GEOS. The dots represent the SLF−CTT combination where the hemispheric contrast is significant with a *p*-value less than 0.05. The color bar indicates the land minus ocean difference for a given SLF−CTT or SLF−CTP bin.

Ground-based remote-sensing studies at selected midlatitude sites [11,12] found a less efficient ice formation in Southern Hemisphere stratiform mixed-phase clouds compared to Northern Hemisphere sites, implying a higher persistence of the liquid phase in the SH. These studies focus on stratiform cloud regimes that may include a range of cloud types and altitudes and do not explicitly isolate low-level stratocumulus clouds. These differences in cloud regime definition and spatial representativeness likely contribute to the apparent mismatch with the hemispheric contrast identified for continental low-level clouds in this study.

The higher SLF observed in continental stratocumulus clouds in the Northern Hemisphere may reflect the combined influence of heterogeneous surface properties and anthropogenic aerosol sources, including variations in land cover, surface temperature, and emission patterns. However, these factors cannot be isolated within the present near-global analysis, and their relative contribution to the hemispheric contrast remains an open question.

CAM6-Oslo shows agreement with AVHRR for stratocumulus clouds over ocean but not over land, while cirrostratus clouds show inconsistent patterns in hemispheric contrasts, with a higher SLF in the SH than in the NH only for SLF < 0.35 when considering statistically significant differences. Comparisons with MODIS indicate agreement for cirrostratus clouds over land and for stratocumulus clouds over both land and ocean (Figure 4, SLF–CTP histograms, last two rows). In contrast, the DYAMOND storm-resolving models generally fail to reproduce the observed hemispheric contrasts over both continental and maritime regions, with only isolated agreement in specific temperature ranges.

The better performance of CAM6-Oslo compared to the DYAMOND models may partly be attributed to the inclusion of interactive aerosol–cloud interactions (see Section 2), which can introduce physically based hemispheric differences in cloud microphysics. However, the precise role of this mechanism in shaping hemispheric SLF differences remains unclear, and the model still does not fully capture the patterns seen in AVHRR for continental stratocumulus clouds. This suggests that the micro- and macrophysics of low-level clouds may be more affected by the Earth's surface than high-level clouds, making the simulation of low-level clouds more complex. Over land, the combined effects of surface heterogeneity, orography, and spatially variable aerosol sources and transport pathways likely contribute to the increased complexity of simulating continental stratocumulus clouds. Isolating the exact mechanisms behind these results would require targeted sensitivity experiments beyond the scope of this study. Although CAM6-Oslo shows reasonable agreement with MODIS for the hemispheric contrast of continental stratocumulus clouds, this agreement breaks down for CTP > 825 hPa, corresponding to warmer cloud-top temperatures. This behavior mirrors the stronger disagreement with AVHRR for CTT > -20 °C.

Hemispheric contrasts in cloud dynamics and cloud microphysics of the simulated cloud types, along with the use of both day and nighttime data and possible seasonal effects influencing results from the DYAMOND datasets (only available for February 2020), may explain the disagreements between the datasets as well as the contrast with the observations. Although high-resolution models better capture turbulence and vertical motion, limitations in the microphysical schemes may still prevent an accurate simulation of mixed-phase clouds. Unfortunately, this study would not benefit from constraining the analysis to observations for February only as the data would be insufficient due to the temporal (daily) and spatial resolution of AVHRR (coarse-grained by using gridboxes) and MODIS.

The absence of a robust hemispheric contrast in the model representation of mixed-phase clouds has also been highlighted by McCoy et al. (2016) [68] in an intercomparison of 26 global climate models. However, their analysis is based on proxy phase metrics derived from temperature-dependent cloud occurrence across the full cloud column, rather than cloud-top properties, and does not distinguish cloud types or surface regimes. These

differences in phase metrics, cloud-region definition, and cloud-type stratification limit the direct comparability with the hemispheric SLF contrasts identified in this study.

4.5. Thermodynamic Dependence of the Liquid Effective Radius in Mixed-Phase Clouds

While SLF–CTT joint histograms primarily capture the thermodynamic dependence of cloud phase partitioning, the SLF–$\overline{r_{liq}}$ diagnostic provides complementary information by explicitly linking phase partitioning to droplet size. As $\overline{r_{liq}}$ is strongly influenced by aerosol loading, condensational growth, and collision–coalescence processes, differences in the SLF–$\overline{r_{liq}}$ relationship across datasets can reveal systematic biases in cloud microphysics schemes that may not be apparent in temperature-based diagnostics alone. This makes the SLF–$\overline{r_{liq}}$ joint histogram a useful benchmark for identifying and interpreting model deficiencies related to mixed-phase cloud microphysics. It allows us to systematically examine how liquid droplet size varies with the supercooled liquid fraction across different cloud types and datasets, highlighting both observed patterns and model-specific behaviors.

Figure 5 shows SLF-$\overline{r_{liq}}$ joint histograms of the different cloud types for AVHRR (a), MODIS (b), CAM6-Oslo (c), and GEOS (d). ICON and SCREAM do not provide information on the effective radius; therefore, these model datasets could not be included in the comparison. Focusing in particular on AVHRR (Figure 5a), the main results can be summarized as follows:

- Low-level and altostratus clouds are more likely to be liquid.
- In altostratus, altocumulus and high-level clouds, $\overline{r_{liq}}$ increases with a low SLF, in agreement with Coopman et al. (2021) [69]. The presence of this trend in cirrus and cirrostratus clouds, which are expected to consist of ice crystals, may be due to a cloud misclassification [50]. In fact, it is worth emphasizing once more that the cloud-type classification relies on the COT–CTP joint histograms. As a result, clouds assigned to the same type can experience different microphysical or dynamical processes depending on their formation region and the prevailing atmospheric conditions. In some cases, this could result in clouds being assigned to an adjacent COT–CTP bin, effectively classifying them as a different cloud type.
- High frequency of $\overline{r_{liq}}$ between 12 and 13 µm is found in stratocumulus and altostratus clouds and is less but still present in cirrostratus clouds, most likely caused by the a priori value assigned to $\overline{r_{liq}}$, which is set to 12 µm [19].

Some limitations have to be considered for AVHRR. In Bruno et al. (2021) [6], a discrepancy in cloud-phase classification between AVHRR-based datasets and the CALIOP (Cloud-Aerosol Lidar with Orthogonal Polarization) dataset was shown: AVHRR retrieved some clouds that CALIOP retrieved as liquid as ice. This concerned 9% of the total collocated cloudy pixels. This indicates that the liquid effective radius may be influenced by errors arising from incorrect phase assignment of cloudy pixels. Stengel et al. (2017) [70] present a validation study comparing several AVHRR datasets, showing that that passive satellite-based products often overestimate the presence of liquid clouds at the expense of ice clouds. The sensitivity of passive retrievals to optically thin ice layers situated above liquid cloud layers is very limited, and the COT filter applied in this study, which excludes clouds with COT < 0.3, may not fully address this issue. Furthermore, some ice particles may still be present within primarily liquid pixels, and the presence of these large ice crystals could bias the retrieved $\overline{r_{liq}}$.

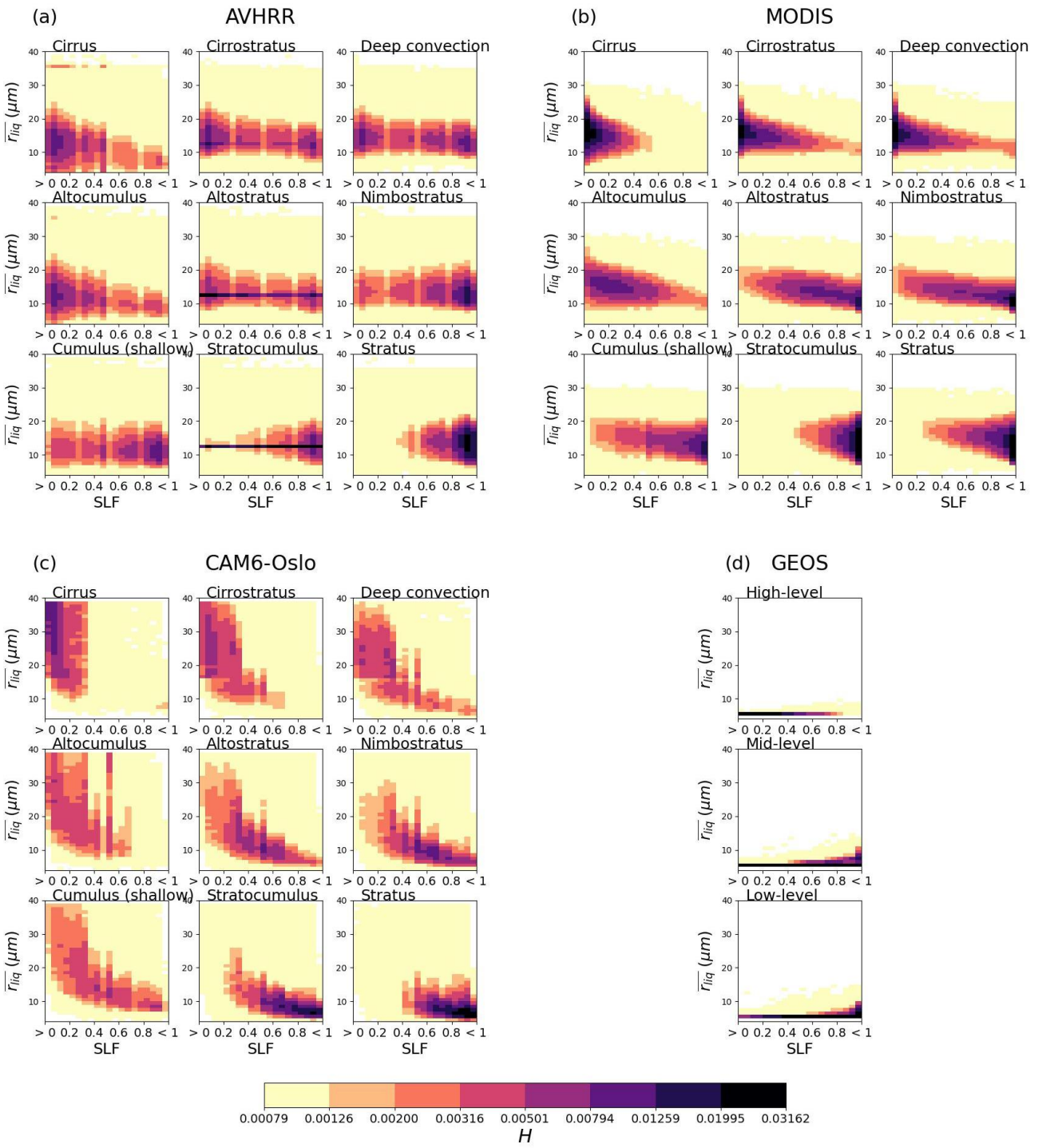

Figure 5. SLF-$\overline{r_{liq}}$ joint histograms of different cloud types in the mixed phase for (**a**) AVHRR, (**b**) MODIS, (**c**) CAM6-Oslo, and (**d**) GEOS.. The color bar indicates the relative frequency of occurrence H (Equation (7)) for a given SLF-$\overline{r_{liq}}$ bin.

Although the histograms of MODIS (Figure 5b) and CAM6-Oslo (Figure 5c) look very different from those of AVHRR, these datasets also exhibit an increase in $\overline{r_{liq}}$ as the SLF decreases for high and mid-level clouds (CAM6-Oslo also for cumulus and stratocumulus clouds and, in general, reaching larger $\overline{r_{liq}}$ values than AVHRR and MODIS). This outcome is likely attributable to the propensity of cold regions, which frequently contain pristine air masses with minimal CCN, enabling the available particles to grow larger than in regions

with higher CCN under equivalent humidity. GEOS (Figure 5d) does not show this trend or the large variability in radius size shown by the other datasets.

Coopman et al. (2020) [71] demonstrated that clouds containing larger droplets tend to glaciate at warmer temperatures. As the SLF decreases from 1 to 0 with decreasing CTT, higher temperatures correspond to SLF values closer to 1, which may explain the observation of smaller $\overline{r_{liq}}$ values when the SLF approaches 1. This behavior can be attributed to several microphysical processes: in clouds with strong updrafts, ice crystals and liquid droplets experience a decrease in temperature with height, and the vapor pressure over ice and over liquid is larger than the in-cloud vapor pressure, leading to the simultaneous growth of liquid droplets and ice crystals at the expense of available water vapor [72]; as parcels ascend within the cloud (where the SLF is expected to decrease due to the lower CTT), droplets may collide and coalesce, leading to larger droplet size [3]; and collisions in the mixed phase temperature range can cause droplets to freeze [73,74] and the formation of secondary ice [75], which may account for the observed decrease in the SLF as $\overline{r_{liq}}$ increases. The satellite retrievals limit the size of the liquid effective radius to 35 µm and 30 µm in AVHRR and MODIS, respectively. This is particularly evident in Figure 5b for MODIS, where the $\overline{r_{liq}}$ size reaches values below 31 µm, although the $\overline{r_{liq}}$ distributions in AVHRR and MODIS are centered on much lower values. In CAM6-Oslo, the $\overline{r_{liq}}$ distribution reaches values up to 39 µm. This difference between the observational datasets and CAM6-Oslo may be due to the possible absence of mechanisms in the cloud microphysics scheme in CAM6-Oslo that should limit droplet growth, although the presence of a fixed maximum $\overline{r_{liq}}$ value in the observational retrievals may also lead to a bias. The decrease in $\overline{r_{liq}}$ with the decrease in the SLF in GEOS may reflect features of the model's cloud parameterization. In addition, the GEOS configuration for the DYAMOND Winter project simulations uses a single-moment cloud microphysics scheme and the Goddard Chemistry Aerosol Radiation and Transport (GOCART) model, in which the aerosol mass of some of the key aerosol types found in the troposphere with their sources, sinks, and transport, are estimated, but the aerosol–cloud interaction is absent, with possible consequences in the simulated $\overline{r_{liq}}$. In addition, CAM6-Oslo clearly shows lower $\overline{r_{liq}}$ in optically thicker clouds. This result may be due to the Twomey effect, wherein an increased aerosol number concentration leads to a larger number of smaller droplets for a given cloud water content, resulting in optically thicker clouds.

4.6. Geographical Distribution of Liquid Droplets in Mixed-Phase Low-Level Clouds

Figures 6 and 7 show the geographical distributions of $\overline{r_{liq}}$ of mixed-phase high- and low-level clouds, respectively, for AVHRR, MODIS, CAM6-Oslo, and GEOS. In both figures, continental clouds in AVHRR and MODIS generally have smaller $\overline{r_{liq}}$ than marine clouds, while this contrast is less pronounced in CAM6-Oslo and absent in GEOS.

Compared to the observations, CAM6-Oslo simulates larger $\overline{r_{liq}}$ in shallow cumulus (Figure 7) and all high-level clouds (Figure 6) and shows lower $\overline{r_{liq}}$ in optically thicker clouds. This result is in line with Figure 5c, and possible reasons for that have been discussed in Section 4.5. GEOS underestimates $\overline{r_{liq}}$ and simulates very uniform distributions. This is probably related, again, to the use of a single-moment microphysics scheme and the absence of aerosol–cloud interaction.

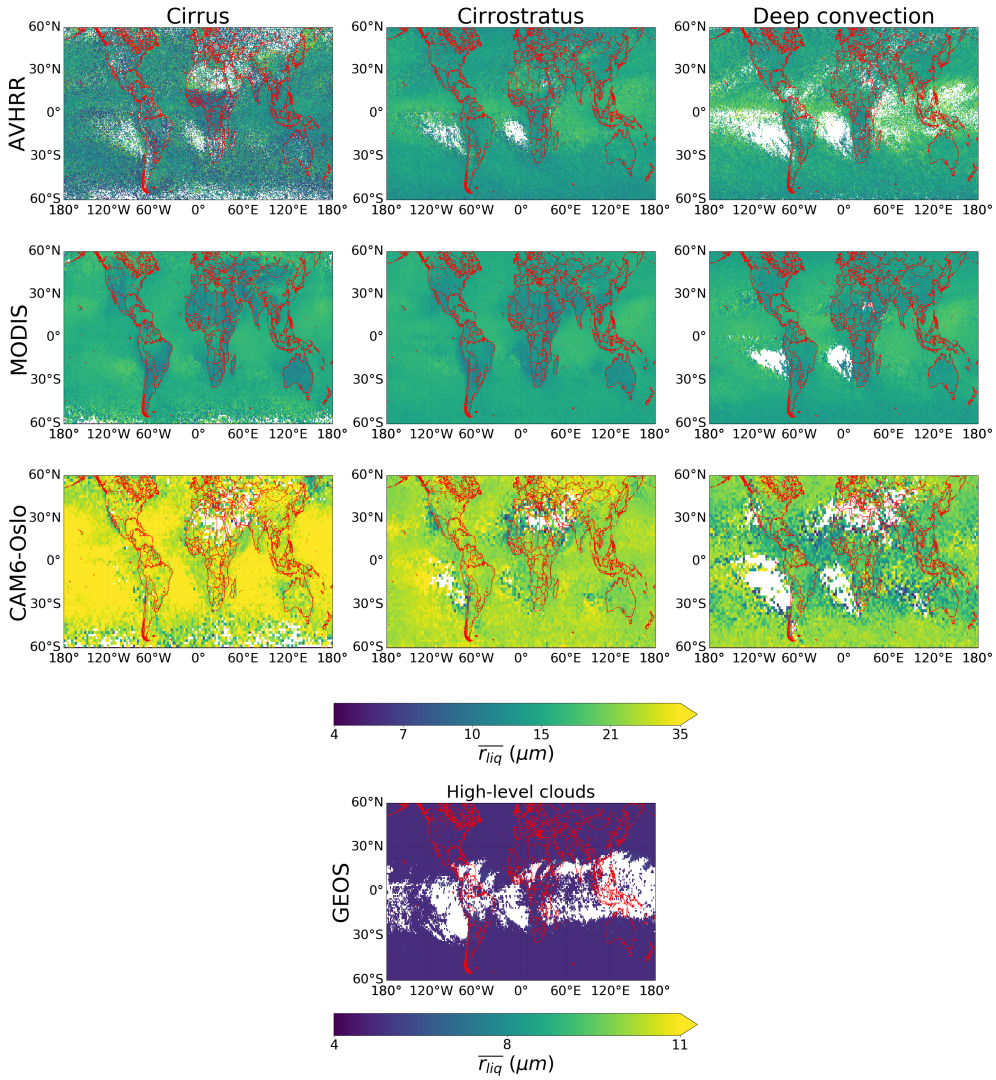

Figure 6. Geographical distribution of $\overline{r_{liq}}$ in cirrus (left), cirrostratus (center), and deep convective (right) clouds in the mixed phase in AVHRR, MODIS, and CAM6-Oslo and in all high-level mixed-phase clouds in GEOS. White pixels indicate no data. Note that the color bar is not linear.

In Figure 7, the observations show larger values of $\overline{r_{liq}}$ also over some mountainous regions, such as the North American Cordillera, the Andes Mountains in South America, and the Himalayas. Among the models, CAM6-Oslo also shows elevated $\overline{r_{liq}}$ over the Andes, whereas GEOS exhibits much less spatial variability in this variable (Figure 7). The locations of enhanced $\overline{r_{liq}}$ are not only dataset-dependent but also vary with cloud type. For instance, in the Southern Hemisphere continental region, AVHRR shows larger droplets in shallow cumulus clouds, whereas in MODIS the largest droplets occur in stratus clouds. Similarly, in the Northern Hemisphere continental region, AVHRR identifies higher $\overline{r_{liq}}$ over northeastern China, while MODIS highlights larger droplets over southern Russia and parts of the eastern coast of China. These differences may be related, again, to the averages in the MODIS retrieval, which also causes the presence of mixed-phase clouds in the tropics (as already discussed in Section 4.2). Lower $\overline{r_{liq}}$ values over land than over the ocean may reflect an indirect effect of the number concentration of aerosols acting as cloud condensation nuclei or ice-nucleating particles, being larger over continental than over maritime regions, leading to greater competition for water vapor among droplets over land than over the ocean [14,76,77]. Higher $\overline{r_{liq}}$ over mountainous areas supports the hypothesis that orographic updrafts may promote droplet growth [3,78], although not all

the mountainous chains show large $\overline{r_{liq}}$. The continental area from 30° to 60° N is larger than the continental area from 30° to 60° S, which is mainly mountainous. Assuming that the presence of larger $\overline{r_{liq}}$ over land in the SH than in the NH for low-level clouds, as seen in AVHRR and partially in MODIS, is valid, the findings of Bruno et al. (2021) [6]—showing a lower SLF over land in the SH than in the NH for the same cloud types—can be explained by the higher likelihood of larger droplets (potentially enhanced by orographic updrafts) colliding and freezing at low temperatures, as well as colliding with ice particles, which may lead to riming and the generation of secondary ice.

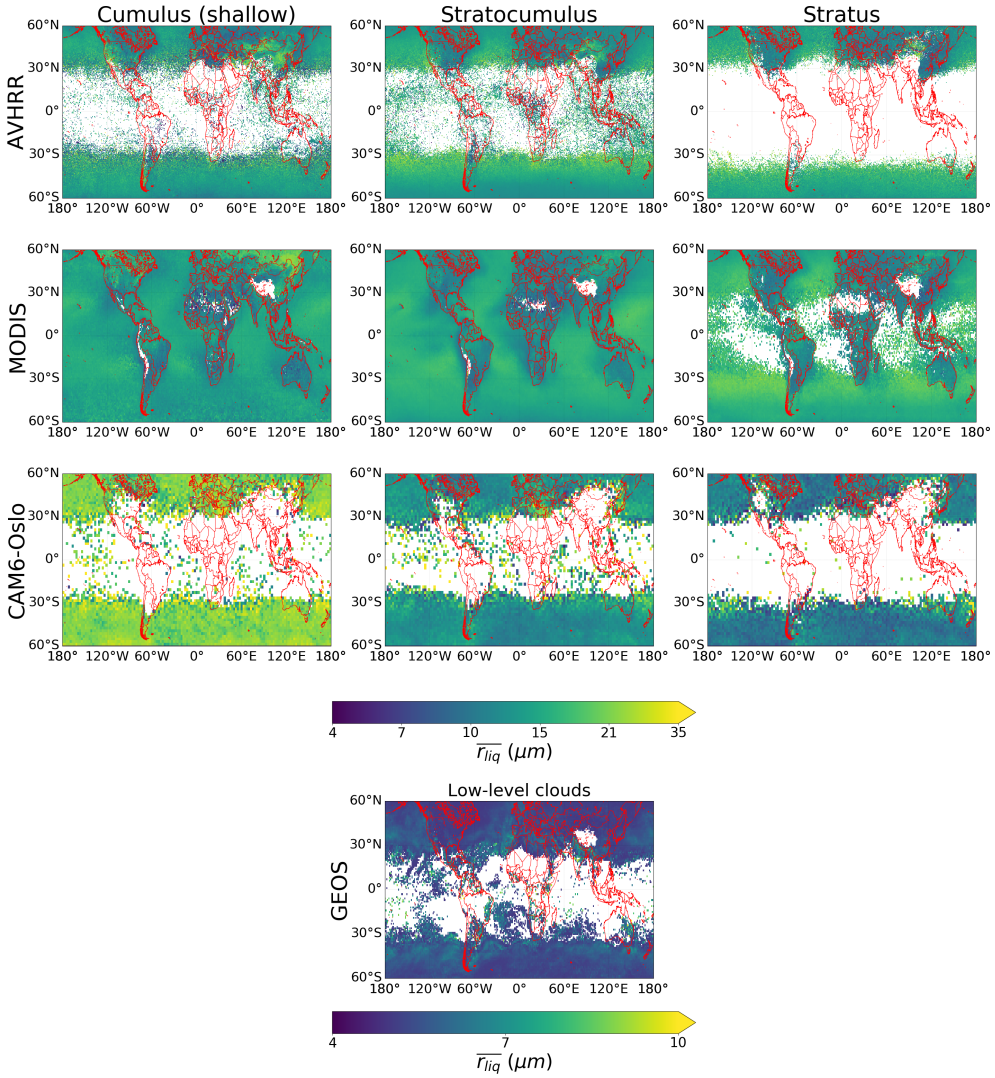

Figure 7. Geographical distribution of $\overline{r_{liq}}$ in shallow cumulus (left), stratocumulus (center), and stratus (right) clouds in the mixed phase in AVHRR, MODIS, and CAM6-Oslo and in all low-level mixed-phase clouds in GEOS. White pixels indicate no data. Note that the color bar is not linear.

While regional features such as enhanced liquid effective radius over major mountain ranges and land–sea contrasts are evident in the observations, the present analysis is not designed to provide a causal attribution at the regional scale. Factors such as local aerosol sources, surface properties, and topography are highly heterogeneous and cannot be disentangled using near-global satellite composites and monthly-averaged model outputs. A detailed assessment of aerosol regimes (e.g., polluted continental regions versus remote marine areas) or surface-type effects would require dedicated regional case studies or targeted model experiments, which are beyond the scope of this work. The patterns

identified here should therefore be interpreted as large-scale statistical signals rather than region-specific causal relationships.

5. Conclusions

In this study, we analyzed near-global (60° N–60° S) observations from passive satellite sensors (AVHRR and MODIS) together with outputs from three storm-resolving models participating in DYAMOND (ICON, SCREAM, and GEOS) and one global climate model (CAM6-Oslo) to assess the representation of cloud-top thermodynamic phase in mixed-phase clouds. The supercooled liquid fraction (SLF) was examined in relation to cloud-top temperature (CTT) and mean liquid effective radius ($\overline{r_{liq}}$) across different cloud types defined using cloud-top pressure and cloud optical thickness thresholds. Particular emphasis was placed on hemispheric midlatitude contrasts and on differences between continental and maritime regions. The main findings are summarized here:

- We derived new reference values for the fraction of mixed-phase clouds up to 60° latitude. While models exhibited a wide spread in occurrence, they generally agreed with observations on their geographical distribution, with mixed-phase clouds mainly located in the midlatitudes.
- Models showed an increase in the SLF with CTT, in agreement with the observations, consistent across cloud types and regions, indicating a robust thermodynamic control on phase partitioning.
- Observations confirmed larger SLF values in the Southern Hemisphere than in the Northern Hemisphere, except for continental stratocumulus, consistent with Bruno et al. (2021) [6]. CAM6-Oslo reproduced these contrasts most closely, while the DYAMOND storm-resolving models showed only limited agreement.
- We introduced SLF–$\overline{r_{liq}}$ joint histograms to link phase partitioning to droplet size. Observations showed an increase in $\overline{r_{liq}}$ as the SLF decreased. CAM6-Oslo reproduced this trend, although with a tendency to overestimate droplet size, while GEOS showed a flatter relationship and less variability.
- Observations show smaller $\overline{r_{liq}}$ over land than over the ocean, whereas models exhibit a less pronounced land/ocean contrast.

Several reasons may explain the disagreements found between models and observations. These include an unrealistic representation of the aerosol influence (especially for low-level clouds) in models and an insufficient representation of the cloud macro- and microphysics in models but also uncertainties in the observational datasets (e.g., the presence of snow in mountainous regions and the use of only one channel in MODIS to retrieve the cloud optical properties may affect the quality of observations), the differences between datasets in SLF computation, and the substantial differences in the satellite retrievals. We have shown that like-for-like comparisons between storm-resolving models and observations are challenging. Future high-resolution modeling experiments could employ satellite simulators or similar tools to enable fairer comparisons between models and observations. Despite these caveats, our results demonstrate that high spatial resolution alone does not guarantee a realistic representation of mixed-phase clouds. In particular, the storm-resolving models considered in our study show difficulties in reproducing observed hemispheric SLF contrasts and land–ocean differences in $\overline{r_{liq}}$. Instead, the inclusion of interactive aerosol–cloud coupling and more advanced cloud microphysics schemes, as implemented in CAM6-Oslo, appears to be a key factor controlling model performance. The systematic inter-model differences identified in hemispheric contrasts and the SLF–$\overline{r_{liq}}$ relationships also have implications for simulated cloud radiative effects since biases in phase partitioning can alter the cloud radiative effect and thus influence modeled climate feedback. By linking supercooled liquid fraction and droplet size, the diagnostic

framework introduced here provides quantitative benchmarks for evaluating and tuning cloud schemes, offering a practical path toward reducing uncertainties in the representation of mixed-phase clouds and their feedback in global and storm-resolving climate models.

Supplementary Materials: The following supporting information can be downloaded at https://www.mdpi.com/article/10.3390/atmos17020156/s1, Figure S1: SLF–CTP joint histograms of mixed-phase clouds for MODIS; Figure S2: SLF–CTP joint histograms of mixed-phase clouds for CAM6–Oslo; Figure S3: SLF–CTT joint histograms of mixed-phase clouds for CAM6-Oslo; Figure S4: SLF–CTT joint histograms of mixed-phase clouds for SCREAM; Figure S5: SLF–CTT joint histograms of mixed-phase clouds for ICON and GEOS; Figure S6: CFAD–like histograms of mixed-phase cirrostratus and stratocumulus in NH and SH over land and ocean, and their hemispheric differences, for AVHRR; Table S1: Relative frequency of occurrence of mixed-phase clouds sorted in cloud types for AVHRR, MODIS, CAM6–Oslo, and SCREAM.

Author Contributions: Conceptualization, O.B. and C.H.; methodology, O.B., J.K.S., and T.S.; software, O.B.; formal analysis, O.B.; investigation, O.B.; data curation, O.B.; writing—original draft preparation, O.B.; writing—review and editing, O.B., C.H., J.K.S., and T.S.; supervision, C.H.; project administration, C.H.; funding acquisition, C.H. All authors have read and agreed to the published version of the manuscript.

Funding: This project has received funding from the European Research Council (ERC) under the European Union's Horizon 2020 research and innovation program under grant agreement No. 714062 (ERC Starting Grant "C2Phase") and No. 758005 (ERC Starting Grant "MC2") and under the Horizon Europe research and innovation program under grant agreement No. 101045273 (ERC Consolidator Grant "STEP-CHANGE"). The projects ESiWACE and ESiWACE2 have received funding from the European Union's Horizon 2020 research and innovation program under grant agreements No. 675191 and 823988. This work used resources of the DKRZ granted by its Scientific Steering Committee (WLA) under project IDs bk1040 and bb1153. J. K. S. was supported by the 2019 Fulbright Student Research Grant and NASA FINESST Grant 80NSSC22K1.

Institutional Review Board Statement: Not applicable.

Data Availability Statement: For the used datasets, the following DOIs provide additional documentation and data download sites: Cloud_cci AVHRR-PMv3—https://doi.org/10.5676/DWD/ESA_Cloud_cci/AVHRR-PM/V003 (accessed on 20 November 2025); MCD06COSP_D3_MODIS—https://doi.org/10.5067/MODIS/MCD06COSP_D3_MODIS.062 (accessed on 20 November 2025); CAM6-Oslo—10.5281/zenodo.10723351. The DYAMOND model outputs supporting the conclusions of this article are archived by the German Climate Computing Centre (DKRZ) and made available through the ESiWACE project (https://www.esiwace.eu/ (accessed on 20 November 2025)).

Acknowledgments: The authors acknowledge support by the state of Baden-Württemberg through bwHPC. DYAMOND data management was provided by the Deutsches Klimarechenzentrum (DKRZ) and supported through the projects ESiWACE and ESiWACE2.

Conflicts of Interest: The authors declare no conflicts of interest.

References

1. Forster, P.; Storelvmo, T.; Armour, K.; Collins, W.; Dufresne, J.L.; Frame, D.; Lunt, D.; Mauritsen, T.; Palmer, M.; Watanabe, M.; et al. The Earth's Energy Budget, Climate Feedbacks, and Climate Sensitivity. In *Climate Change 2021: The Physical Science Basis. Contribution of Working Group I to the Sixth Assessment Report of the Intergovernmental Panel on Climate Change*; Masson-Delmotte, V., Zhai, P., Pirani, A., Connors, S., Péan, C., Berger, S., Caud, N., Chen, Y., Goldfarb, L., Gomis, M., et al., Eds.; Cambridge University Press: Cambridge, UK; New York, NY, USA, 2021; pp. 923–1054. https://doi.org/10.1017/9781009157896.009.
2. Korolev, A.; DeMott, P.J.; Heckman, I.; Wolde, M.; Williams, E.; Smalley, D.J.; Donovan, M.F. Observation of secondary ice production in clouds at low temperatures. *Atmos. Chem. Phys.* **2022**, *22*, 13103–13113. https://doi.org/10.5194/acp-22-13103-2022.
3. Lamb, D.; Verlinde, J. *Physics and Chemistry of Clouds*; Cambridge University Press: Cambridge, UK, 2011.
4. Cesana, G.; Storelvmo, T. Improving climate projections by understanding how cloud phase affects radiation. *J. Geophys. Res.* **2017**, *122*, 4594–4599. https://doi.org/10.1002/2017JD026927.

5. Tan, I.; Storelvmo, T.; Choi, Y.S. Spaceborne lidar observations of the ice-nucleating potential of dust, polluted dust, and smoke aerosols in mixed-phase clouds. *J. Geophys. Res.* **2014**, *119*, 6653–6665. https://doi.org/10.1002/2013JD021333.
6. Bruno, O.; Hoose, C.; Storelvmo, T.; Coopman, Q.; Stengel, M. Exploring the Cloud Top Phase Partitioning in Different Cloud Types Using Active and Passive Satellite Sensors. *Geophys. Res. Lett.* **2021**, *48*, e2020GL089863. https://doi.org/10.1029/2020GL089863.
7. Nagao, T.M.; Suzuki, K. Characterizing Vertical Stratification of the Cloud Thermodynamic Phase with a Combined Use of CALIPSO Lidar and MODIS SWIR Measurements. *J. Geophys. Res. Atmos.* **2022**, *127*, e2022JD036826. https://doi.org/10.1029/2022JD036826.
8. Suzuki, K.; Nagao, T.M.; Murai, A. Satellite-Based Diagnostics of Precipitation Process in Mixed-Phase Clouds: Extension from Warm Rain Process Statistics. *Geophys. Res. Lett.* **2024**, *51*, e2024GL110573. https://doi.org/10.1029/2024GL110573.
9. Villanueva, D.; Heinold, B.; Seifert, P.; Deneke, H.; Radenz, M.; Tegen, I. The day-to-day co-variability between mineral dust and cloud glaciation: A proxy for heterogeneous freezing. *Atmos. Chem. Phys.* **2020**, *20*, 2177–2199. https://doi.org/10.5194/acp-20-2177-2020.
10. Villanueva, D.; Neubauer, D.; Gasparini, B.; Ickes, L.; Tegen, I. Constraining the Impact of Dust-Driven Droplet Freezing on Climate Using Cloud-Top-Phase Observations. *Geophys. Res. Lett.* **2021**, *48*, e2021GL092687. https://doi.org/10.1029/2021GL092687.
11. Kanitz, T.; Seifert, P.; Ansmann, A.; Engelmann, R.; Althausen, D.; Casiccia, C.; Rohwer, E.G. Contrasting the impact of aerosols at northern and southern midlatitudes on heterogeneous ice formation. *Geophys. Res. Lett.* **2011**, *38*, L17802. https://doi.org/10.1029/2011GL048532.
12. Radenz, M.; Bühl, J.; Seifert, P.; Baars, H.; Engelmann, R.; Barja González, B.; Mamouri, R.E.; Zamorano, F.; Ansmann, A. Hemispheric contrasts in ice formation in stratiform mixed-phase clouds: Disentangling the role of aerosol and dynamics with ground-based remote sensing. *Atmos. Chem. Phys.* **2021**, *21*, 17969–17994. https://doi.org/10.5194/acp-21-17969-2021.
13. Yang, C.A.; Diao, M.; Shi, Y.; Liu, X. Hemispheric Asymmetry of Phase Partition in Mixed-Phase Clouds Based on Near Global-Scale Airborne Observations. *Geophys. Res. Lett.* **2025**, *52*, e2025GL115946. https://doi.org/10.1029/2025GL115946.
14. Lohmann, U.; Feichter, J. Global indirect aerosol effects: A review. *Atmos. Chem. Phys.* **2005**, *5*, 715–737. https://doi.org/10.5194/acp-5-715-2005.
15. McCoy, D.T.; Burrows, S.M.; Wood, R.; Grosvenor, D.P.; Elliott, S.M.; Ma, P.L.; Rasch, P.J.; Hartmann, D.L. Natural aerosols explain seasonal and spatial patterns of Southern Ocean cloud albedo. *Sci. Adv.* **2015**, *1*, e1500157. https://doi.org/10.1126/sciadv.1500157.
16. Vergara-Temprado, J.; Miltenberger, A.K.; Furtado, K.; Grosvenor, D.P.; Shipway, B.J.; Hill, A.A.; Wilkinson, J.M.; Field, P.R.; Murray, B.J.; Carslaw, K.S. Strong control of Southern Ocean cloud reflectivity by ice-nucleating particles. *Proc. Natl. Acad. Sci. USA* **2018**, *115*, 2687–2692. https://doi.org/10.1073/pnas.1721627115.
17. Cesana, G.; Waliser, D.E.; Jiang, X.; Li, J.L.F. Multimodel evaluation of cloud phase transition using satellite and reanalysis data. *J. Geophys. Res. Atmos.* **2015**, *120*, 7871–7892. https://doi.org/10.1002/2014JD022932.
18. Stengel, M.; Stapelberg, S.; Sus, O.; Finkensieper, S.; Würzler, B.; Philipp, D.; Hollmann, R.; Poulsen, C.; Christensen, M.; McGarragh, G. Cloud_cci Advanced Very High Resolution Radiometer post meridiem (AVHRR-PM) dataset version 3: 35-year climatology of global cloud and radiation properties. *Earth Syst. Sci. Data* **2020**, *12*, 41–60. https://doi.org/10.5194/essd-12-41-2020.
19. Thomas, G.E.; Poulsen, C.A.; Siddans, R.; Povey, A.; Prata, A.T.; Philipp, D.; Stengel, M.; Proud, S.; McGarragh, G.; Schlundt, C.; et al. ATBD-CC4CLv6.2. In *ESA Cloud_cci Algorithm Theoretical Baseline Document v9.0 Community Cloud Retrieval for Climate (CC4CL)*; ESA's Climate: Harwell, UK, 2023.
20. Pincus, R.; Hubanks, P.A.; Platnick, S.; Meyer, K.; Holz, R.E.; Botambekov, D.; Wall, C.J. Updated observations of clouds by MODIS for global model assessment. *Earth Syst. Sci. Data* **2023**, *15*, 2483–2497. https://doi.org/10.5194/essd-15-2483-2023.
21. NASA. *MCD06COSP_M3_MODIS—MODIS (Aqua/Terra) Cloud Properties Level 3 Monthly, 1x1 Degree Grid*; NASA: Washington, DC, USA, 2022. https://doi.org/10.5067/MODIS/MCD06COSP_D3_MODIS.062.
22. Bodas-Salcedo, A.; Webb, M.J.; Bony, S.; Chepfer, H.; Dufresne, J.L.; Klein, S.A.; Zhang, Y.; Marchand, R.; Haynes, J.M.; Pincus, R.; et al. COSP: Satellite simulation software for model assessment. *Bull. Am. Meteorol. Soc.* **2011**, *92*, 1023–1043. https://doi.org/10.1175/2011BAMS2856.1.
23. Seland, Ø.; Bentsen, M.; Olivié, D.; Toniazzo, T.; Gjermundsen, A.; Graff, L.S.; Debernard, J.B.; Gupta, A.K.; He, Y.C.; Kirkevåg, A.; et al. Overview of the Norwegian Earth System Model (NorESM2) and key climate response of CMIP6 DECK, historical, and scenario simulations. *Geosci. Model Dev.* **2020**, *13*, 6165–6200. https://doi.org/10.5194/gmd-13-6165-2020.
24. Kirkevåg, A.; Iversen, T.; Seland, Ø.; Hoose, C.; Kristjánsson, J.E.; Struthers, H.; Ekman, A.M.L.; Ghan, S.; Griesfeller, J.; Nilsson, E.D.; et al. Aerosol–climate interactions in the Norwegian Earth System Model–NorESM1-M. *Geosci. Model Dev.* **2013**, *6*, 207–244.
25. Kirkevåg, A.; Grini, A.; Olivié, D.; Seland, Ø.; Alterskjær, K.; Hummel, M.; Karset, I.H.H.; Lewinschal, A.; Liu, X.; Makkonen, R.; et al. A production-tagged aerosol module for Earth system models, OsloAero5.3—Extensions and updates for CAM5.3-Oslo. *Geosci. Model Dev.* **2018**, *11*, 3945–3982.
26. Stevens, B.; Satoh, M.; Auger, L.; Biercamp, J.; Bretherton, C.S.; Chen, X.; Düben, P.; Judt, F.; Khairoutdinov, M.; Klocke, D.; et al. DYAMOND: The DYnamics of the Atmospheric general circulation Modeled On Non-hydrostatic Domains. *Prog. Earth Planet. Sci.* **2019**, *6*, 61. https://doi.org/10.1186/s40645-019-0304-z.

27. Reinert, D.; Prill, F.; Frank, H.; Denhard, M.; Baldauf, M.; Schraff, C.; Gebhardt, C.; Marsigli, C.; Zängl, G. *DWD Database Reference for the Global and Regional ICON and ICON-EPS Forecasting System*; Deutscher Wetterdienst: Offenbach, Germany, 2023.
28. Zängl, G.; Reinert, D.; Rípodas, P.; Baldauf, M. The ICON (ICOsahedral Non-hydrostatic) modelling framework of DWD and MPI-M: Description of the non-hydrostatic dynamical core. *Q. J. R. Meteorol. Soc.* **2015**, *141*, 563–579. https://doi.org/10.1002/qj.2378.
29. Caldwell, P.M.; Terai, C.R.; Hillman, B.; Keen, N.D.; Bogenschutz, P.; Lin, W.; Beydoun, H.; Taylor, M.; Bertagna, L.; Bradley, A.M.; et al. Convection-Permitting Simulations with the E3SM Global Atmosphere Model. *J. Adv. Model. Earth Syst.* **2021**, *13*, e2021MS002544. https://doi.org/10.1029/2021MS002544.
30. Putman, W.M.; Suarez, M. Cloud-system resolving simulations with the NASA Goddard Earth Observing System global atmospheric model (GEOS-5). *Geophys. Res. Lett.* **2011**, *38*, L16809. https://doi.org/10.1029/2011GL048438.
31. King, M.D.; Platnick, S.; Yang, P.; Arnold, G.T.; Gray, M.A.; Riedi, J.C.; Ackerman, S.A.; Liou, K.N. Remote sensing of liquid water and ice cloud optical thickness and effective radius in the Arctic: Application of airborne multispectral MAS data. *J. Atmos. Ocean. Technol.* **2004**, *21*, 857–875. https://doi.org/10.1175/1520-0426(2004)021<0857:RSOLWA>2.0.CO;2.
32. Grosvenor, D.P.; Wood, R. The effect of solar zenith angle on MODIS cloud optical and microphysical retrievals within marine liquid water clouds. *Atmos. Chem. Phys.* **2014**, *14*, 7291–7321. https://doi.org/10.5194/acp-14-7291-2014.
33. Costa-Surós, M.; Sourdeval, O.; Acquistapace, C.; Baars, H.; Carbajal Henken, C.; Genz, C.; Hesemann, J.; Jimenez, C.; König, M.; Kretzschmar, J.; et al. Detection and attribution of aerosol–cloud interactions in large-domain large-eddy simulations with the ICOsahedral Non-hydrostatic model. *Atmos. Chem. Phys.* **2020**, *20*, 5657–5678. https://doi.org/10.5194/acp-20-5657-2020.
34. Stengel, M.; Mieruch, S.; Jerg, M.; Karlsson, K.G.; Scheirer, R.; Maddux, B.; Meirink, J.; Poulsen, C.; Siddans, R.; Walther, A.; et al. The Clouds Climate Change Initiative: Assessment of state-of-the-art cloud property retrieval schemes applied to AVHRR heritage measurements. *Remote Sens. Environ.* **2015**, *162*, 363–379. https://doi.org/10.1016/j.rse.2013.10.035.
35. Hoose, C.; Karrer, M.; Barthlott, C. Cloud Top Phase Distributions of Simulated Deep Convective Clouds. *J. Geophys. Res. Atmos.* **2018**, *123*, 10,464–10,476. https://doi.org/10.1029/2018JD028381.
36. Norris, J.R.; Weaver, C.P. Improved Techniques for Evaluating GCM Cloudiness Applied to the NCAR CCM3. *J. Clim.* **2001**, *14*, 2540–2550. https://doi.org/10.1175/1520-0442(2001)014<2540:ITFEGC>2.0.CO;2.
37. Bony, S.; Dufresne, J.L.; Le Treut, H.; Morcrette, J.J.; Senior, C. On dynamic and thermodynamic components of cloud changes. *Clim. Dyn.* **2004**, *22*, 71–86. https://doi.org/10.1007/s00382-003-0369-6.
38. Tselioudis, G.; Zhang, Y.; Rossow, W.B. Cloud and Radiation Variations Associated with Northern Midlatitude Low and High Sea Level Pressure Regimes. *J. Clim.* **2000**, *13*, 312–327. https://doi.org/10.1175/1520-0442(2000)013<0312:CARVAW>2.0.CO;2.
39. Ringer, M.A.; Allan, R.P. Evaluating climate model simulations of tropical cloud. *Tellus A* **2004**, *56*, 308–327. https://doi.org/10.3402/tellusa.v56i4.14419.
40. Williams, K.; Ringer, M.; Senior, C. Evaluating the cloud response to climate change and current climate variability. *Clim. Dyn.* **2003**, *20*, 705–721. https://doi.org/10.1007/s00382-002-0303-3.
41. Williams, K.D.; Ringer, M.A.; Senior, C.A.; Webb, M.J.; McAvaney, B.J.; Andronova, N.; Bony, S.; Dufresne, J.L.; Emori, S.; Gudgel, R.; et al. Evaluation of a component of the cloud response to climate change in an intercomparison of climate models. *Clim. Dyn.* **2006**, *26*, 145–165. https://doi.org/10.1007/s00382-005-0067-7.
42. Jakob, C.; Tselioudis, G. Objective identification of cloud regimes in the Tropical Western Pacific. *Geophys. Res. Lett.* **2003**, *30*, 2082. https://doi.org/10.1029/2003GL018367.
43. Rossow, W.B.; Tselioudis, G.; Polak, A.; Jakob, C. Tropical climate described as a distribution of weather states indicated by distinct mesoscale cloud property mixtures. *Geophys. Res. Lett.* **2005**, *32*, L21812. https://doi.org/10.1029/2005GL024584.
44. Williams, K.D.; Senior, C.A.; Slingo, A.; Mitchell, J.F.B. Towards evaluating cloud response to climate change using clustering technique identification of cloud regimes. *Clim. Dyn.* **2005**, *24*, 701–719. https://doi.org/10.1007/s00382-004-0512-z.
45. Williams, K.D.; Tselioudis, G. GCM intercomparison of global cloud regimes: Present-day evaluation and climate change response. *Clim. Dyn.* **2007**, *29*, 231–250. https://doi.org/10.1007/s00382-007-0232-2.
46. Oreopoulos, L.; Cho, N.; Lee, D. Using MODIS cloud regimes to sort diagnostic signals of aerosol-cloud-precipitation interactions. *J. Geophys. Res. Atmos.* **2017**, *122*, 5416–5440. https://doi.org/10.1002/2016JD026120.
47. Schuddeboom, A.; McDonald, A.J.; Morgenstern, O.; Harvey, M.; Parsons, S. Regional Regime-Based Evaluation of Present-Day General Circulation Model Cloud Simulations Using Self-Organizing Maps. *J. Geophys. Res. Atmos.* **2018**, *123*, 4259–4272. https://doi.org/10.1002/2017JD028196.
48. Zhang, W.; Wang, J.; Jin, D.; Oreopoulos, L.; Zhang, Z. A Deterministic Self-Organizing Map Approach and its Application on Satellite Data based Cloud Type Classification. In *Proceedings of the 2018 IEEE International Conference on Big Data, Big Data, Seattle, WA, USA, 10–13 December 2018*; IEEE: Piscataway, NJ, USA; pp. 2027–2034. https://doi.org/10.1109/BigData.2018.8622558.
49. Rossow, W.B.; Schiffer, R.A. Advances in Understanding Clouds from ISCCP. *Bull. Am. Meteorol. Soc.* **1999**, *80*, 2261–2288. https://doi.org/10.1175/1520-0477(1999)080<2261:AIUCFI>2.0.CO;2.
50. Hahn, C.J.; Rossow, W.B.; Warren, S.G. ISCCP Cloud Properties Associated with Standard Cloud Types Identified in Individual Surface Observations. *J. Clim.* **2001**, *14*, 11–28. https://doi.org/10.1175/1520-0442(2001)014<0011:ICPAWS>2.0.CO;2.

51. Anderberg, M.R. *Cluster Analysis for Applications*; Academic Press: New York, NY, USA, 1973; p. 359. https://doi.org/10.1137/1017065.
52. Fränti, P.; Sieranoja, S. How much k-means can be improved by using better initialization and repeats? *Pattern Recognit.* **2019**, *93*, 95–112. https://doi.org/10.1016/j.patcog.2019.04.014.
53. Yuter, S.E.; Houze, R.A. Three-Dimensional Kinematic and Microphysical Evolution of Florida Cumulonimbus. Part II: Frequency Distributions of Vertical Velocity, Reflectivity, and Differential Reflectivity. *Mon. Weather. Rev.* **1995**, *123*, 1941–1963. https://doi.org/10.1175/1520-0493(1995)123<1941:TDKAME>2.0.CO;2.
54. Fu, Y.; Lin, Y.; Liu, G.; Wang, Q. Seasonal characteristics of precipitation in 1998 over East Asia as derived from TRMM PR. *Adv. Atmos. Sci.* **2003**, *20*, 511–529. https://doi.org/10.1007/BF02915495.
55. Chen, T.; Guo, J.; Li, Z.; Zhao, C.; Liu, H.; Cribb, M.; Wang, F.; He, J. A CloudSat Perspective on the Cloud Climatology and Its Association with Aerosol Perturbations in the Vertical over Eastern China. *J. Atmos. Sci.* **2016**, *73*, 3599–3616. https://doi.org/10.1175/JAS-D-15-0309.1.
56. Ewald, F.; Zinner, T.; Kölling, T.; Mayer, B. Remote sensing of cloud droplet radius profiles using solar reflectance from cloud sides—Part 1: Retrieval development and characterization. *Atmos. Meas. Tech.* **2019**, *12*, 1183–1206. https://doi.org/10.5194/amt-12-1183-2019.
57. Shen, C.; Li, G.; Dong, Y. Vertical Structures Associated with Orographic Precipitation during Warm Season in the Sichuan Basin and Its Surrounding Areas at Different Altitudes from 8-Year GPM DPR Observations. *Remote Sens.* **2022**, *14*, 4222. https://doi.org/10.3390/rs14174222.
58. Fisher, R. *Statistical Methods for Research Workers*; Biological monographs and manuals; Oliver and Boyd: Edinburgh, UK, 1925.
59. PVIR. *Product Validation and Intercomparison Report (PVIR)—ESA Cloud_cci*; ESA's Climate: Harwell, UK, 2020.
60. Tan, J.; Oreopoulos, L.; Jakob, C.; Jin, D. Evaluating rainfall errors in global climate models through cloud regimes. *Clim. Dyn.* **2018**, *50*, 3301–3314. https://doi.org/10.1007/s00382-017-3806-7.
61. Cesana, G.; Chepfer, H. How well do climate models simulate cloud vertical structure? A comparison between CALIPSO-GOCCP satellite observations and CMIP5 models. *Geophys. Res. Lett.* **2012**, *39*, 20803. https://doi.org/10.1029/2012GL053153.
62. Cesana, G.; Waliser, D.E. Characterizing and understanding systematic biases in the vertical structure of clouds in CMIP5/CFMIP2 models. *Geophys. Res. Lett.* **2016**, *43*, 10538–10546. https://doi.org/10.1002/2016GL070515.
63. Luo, H.; Quaas, J.; Han, Y. Examining cloud vertical structure and radiative effects from satellite retrievals and evaluation of CMIP6 scenarios. *Atmos. Chem. Phys.* **2023**, *23*, 8169–8186. https://doi.org/10.5194/acp-23-8169-2023.
64. Korolev, A.V.; McFarquhar, G.; Field, P.R.; Franklin, C.; Lawson, P.; Wang, Z.; Williams, E.; Abel, S.J.; Axisa, D.; Borrmann, S.; et al. Mixed-Phase Clouds: Progress and Challenges. *Meteorol. Monogr.* **2017**, *58*, 5.1–5.50. https://doi.org/10.1175/AMSMONOGRAPHS-D-17-0001.1.
65. Hu, Y.; Rodier, S.; Xu, K.m.; Sun, W.; Huang, J.; Lin, B.; Zhai, P.; Josset, D. Occurrence, liquid water content, and fraction of supercooled water clouds from combined CALIOP/IIR/MODIS measurements. *J. Geophys. Res. Atmos.* **2010**, *115*, D00H34. https://doi.org/10.1029/2009JD012384.
66. Korolev, A.; Milbrandt, J. How Are Mixed-Phase Clouds Mixed? *Geophys. Res. Lett.* **2022**, *49*, e2022GL099578. https://doi.org/10.1029/2022GL099578.
67. Sassen, K. Evidence for Liquid-Phase Cirrus Cloud Formation from Volcanic Aerosols: Climatic Implications. *Science* **1992**, *257*, 516–519. https://doi.org/10.1126/science.257.5069.516.
68. McCoy, D.T.; Tan, I.; Hartmann, D.L.; Zelinka, M.D.; Storelvmo, T. On the relationships among cloud cover, mixed-phase partitioning, and planetary albedo in GCMs. *J. Adv. Model. Earth Syst.* **2016**, *8*, 650–668. https://doi.org/10.1002/2015MS000589.
69. Coopman, Q.; Hoose, C.; Stengel, M. Analyzing the Thermodynamic Phase Partitioning of Mixed Phase Clouds Over the Southern Ocean Using Passive Satellite Observations. *Geophys. Res. Lett.* **2021**, *48*, e2021GL093225. https://doi.org/10.1029/2021GL093225.
70. Stengel, M.; Stapelberg, S.; Sus, O.; Schlundt, C.; Poulsen, C.; Thomas, G.; Christensen, M.; Henken, C.C.; Preusker, R.; Fischer, J.; et al. Cloud property datasets retrieved from AVHRR, MODIS, AATSR and MERIS in the framework of the Cloud-cci project. *Earth Syst. Sci. Data* **2017**, *9*, 881–904. https://doi.org/10.5194/essd-9-881-2017.
71. Coopman, Q.; Riedi, J.; Zeng, S.; Garrett, T.J. Space-Based Analysis of the Cloud Thermodynamic Phase Transition for Varying Microphysical and Meteorological Regimes. *Geophys. Res. Lett.* **2020**, *47*, e2020GL087122. https://doi.org/10.1029/2020GL087122.
72. Korolev, A.V.; Mazin, I.P. Supersaturation of Water Vapor in Clouds. *J. Atmos. Sci.* **2003**, *60*, 2957–2974. https://doi.org/10.1175/1520-0469(2003)060<2957:SOWVIC>2.0.CO;2.
73. Hobbs, P.V. The Aggregation of Ice Particles in Clouds and Fogs at Low Temperatures. *J. Atmos. Sci.* **1965**, *22*, 296–300. https://doi.org/10.1175/1520-0469(1965)022<0296:TAOIPI>2.0.CO;2.
74. Czys, R.R. Ice Initiation by Collision-Freezing in Warm-Based Cumuli. *J. Appl. Meteorol. (1988–2005)* **1989**, *28*, 1098–1104.
75. Korolev, A.; Leisner, T. Review of experimental studies of secondary ice production. *Atmos. Chem. Phys.* **2020**, *20*, 11767–11797. https://doi.org/10.5194/acp-20-11767-2020.

76. Twomey, S. The Influence of Pollution on the Shortwave Albedo of Clouds. *J. Atmos. Sci.* **1977**, *34*, 1149–1152. https://doi.org/10.1175/1520-0469(1977)034<1149:TIOPOT>2.0.CO;2.
77. Andreae, M.; Rosenfeld, D. Aerosol–cloud–precipitation interactions. Part 1. The nature and sources of cloud-active aerosols. *Earth-Sci. Rev.* **2008**, *89*, 13–41. https://doi.org/10.1016/j.earscirev.2008.03.001.
78. Houze, R.A., Jr. Orographic effects on precipitating clouds. *Rev. Geophys.* **2012**, *50*, RG1001. https://doi.org/10.1029/2011RG000365.